This is to certify that the

thesis entitled

EFFECTS OF THE LASER BEAM POWDER WELDING PROCESS
ON THE HARDENABILITY OF
SUPERALLOY IN-738LC DEPOSITION WELDS

presented by

Jose Humberto Garcia Buitrago

has been accepted towards fulfillment
of the requirements for

Master's degree in Materials Science

K. Mukherjee
Major professor

Date November 16, 1995

EFFECTS OF THE LASER BEAM POWDER WELDING PROCESS ON THE HARDENABILITY OF SUPERALLOY IN-738LC DEPOSITION WELDS

By

José Humberto García Buitrago

A THESIS

Submitted to
Michigan State University
in partial fulfillment of the requirements
for the degree of

MASTER OF SCIENCE

Department of Materials Science and Mechanics

1995

ABSTRACT

EFFECTS OF THE LASER BEAM POWDER WELDING PROCESS
ON THE HARDENABILITY OF
SUPERALLOY IN-738LC DEPOSITION WELDS

By

José Humberto García Buitrago

The repair-welding of superalloy gas turbine parts is presently limited to low stress bearing areas, because their complex metallurgy makes them susceptible to formation of discontinuities and to disruption in the element and phase distribution. To extend repairs to highly stressed areas and increase the recoverability of serviced parts, it would be necessary to ensure that the weld deposit attains the same metallurgical characteristics as the original superalloy component.

This research studied the metallurgical response of the cast nickel-based superalloy IN-738LC to the laser beam powder welding process, by quantifying the discontinuities and analyzing the element distribution and microstructure of the weld deposit and substrate, before and after the hardening heat treatments. It was found that the alloy attains proper size, shape and distribution of the strengthening precipitate phase (γ'), but a different intergranular carbide distribution. This condition is expected to produce equivalent low temperature tensile properties, but diminished creep-rupture properties, as compared with the heat treated cast material.

ACKNOWLEDGMENTS

The author wishes to express his gratitude to Lagoven, S. A. for their total financial support during the author's stay at Michigan State University.

Appreciation is also extended to my thesis advisor, Dr. Kali Mukherjee, for his academic guidance, which allowed me to fulfill an important educational experience. I would also like to thank Dr. Thomas Bieler and Dr. James Lucas for their suggestions for improving this thesis.

The topic for this project was an outcome of the author's acquaintance with Marcial Trujillo from Chromalloy Heavy Industrial Turbine, Dallas, Texas. My sincere thanks to him and Chromalloy HIT for their support in the experimental stages of the research.

Appreciation is also due to my wife, Carmen María, for her assistance in the final preparation of the thesis write-up, as well as for her patience and understanding.

Finally, a very special thanks to my mother, for her prayers and encouragement, and above all, thanks to God.

TABLE OF CONTENT

LIST OF TABLES

LIST OF FIGURES

CHAPTER 1

INTRODUCTION

1.1- BACKGROUND AND MOTIVATION

Superalloys, which successfully perform at a higher fraction of their actual melting point than other metallurgical materials, make possible much of the high-temperature engineering technology.

Superalloys are used widely for the fabrication of gas turbine parts, for both aviation and industrial service. Also these alloys are used to a lesser degree for the fabrication of components for rocket engines, as well as oil refining and petrochemical equipment. The reason for its use in gas turbines is that the efficiency and performance of these types of engines are proportional to the firing temperature and rotor speed, which impose high temperatures and stresses to the internal components, specially the rotating parts that are exposed to the hot gas path.

Even though superalloys are environmental resistant and have good mechanical strength, gas turbine components are eventually affected by time dependent damage mechanisms, such as hot corrosion, aging, creep and fatigue, as well as contact damage such as impact by foreign objects, erosion and seal rubbing (**1**). For industrial gas turbines, two of the major damage modes appear to be related to hot corrosion and impact by foreign objects (**2**), which involve actual material loss.

In order to maintain the reliability and performance of gas turbines, periodic overhauls are established to correct service damage and degradation. However, because of the high cost of the replacement parts, there is a considerable incentive to repair rather than replace the affected parts (**3**). In the case of rotor blades, refurbishment may involve welding, thermo-mechanical treatments such as hot isostatic pressing (HIP) and recoating, among other processes (**4**).

Due to the complex metallurgy of superalloys, the repair-welding needed to rebuild material loss and eliminate thermal and fatigue cracking presents major difficulties. The most widely practiced method for weld build-up consists of using manual gas tungsten arc welding (GTAW) techniques; however, the application of each layer of material requires great dexterity, control and concentration of skilled welders, as well as special heat-sink fixturing to minimize the effect of heat input on the base material. Even though precautions are taken, the reproducibility for manually welded blades is low, and thus the rejection rate can be high (**3**).

One way to minimize problems with GTAW methods is to use low heat input processes such as laser beam welding, which is also compatible with automation. Laser beam welding technology has been proven successfully in many commercial alloys including carbon and alloy steels, stainless steels and aluminum alloys. There have also been some successful applications on solid solution hardened superalloys such as Inconel 625 and Hastelloy X* , and precipitation hardened alloys such as Inconel alloys 713, 718** and Cabot Alloy 214*** , among others (**5, 6, 7, 8**). However, the weldability of these materials is still considered to be low due to their high susceptibility to cracking, and the strength of the weld deposits have generally been found to be lower than the base material (**5, 9, 10**).

---

* Hastelloy is a trademark of Haynes International

** Inconel is a trademark of INCO Alloys, International

*** Cabot is a trademark of Cabot Corp.

In order to ensure high quality welds and avoid service failure, the industrial repair of superalloy parts has been restricted to static components such as combustion liners, fuel nozzles and stationary vanes, and to low stress bearing areas of rotating parts such as platform Z-notches, uppermost sections of airfoils and seal faces of blades , as well as balance rings on discs (**8**). By limiting the repairs to low stress areas, the welds can be done with filler alloys of lower strength than the base metal, which offer higher weldability and reduce the possibility of defects.

To extend the repair to highly stressed areas, it would be necessary to ensure that the alloy deposited by laser beam fusion can attain the same metallurgical characteristics as the superalloy substrate. A properly hardened superalloy presents an optimal balance between intragranular and grain boundary strength, that is achieved by providing solid solution strengthening to the matrix and controlling the size, shape and distribution of the precipitation hardening phases. Additionally, high fatigue resistance and creep strength are enhanced by controlling the size and orientation of the grains.

In general, the response of superalloys to laser beam processing depends upon rapid solidification effects in the weld pool, high temperature gradient effects in the heat affected zone (HAZ) and element vaporization due to the high temperatures associated with the process. These effects alter the very specialized element and phase distribution responsible for the material strength, and may also produce strain-age cracking or hot micro-cracking in the HAZ. The former cracking phenomenon is associated with the inability of the material to relieve residual stresses due to its high creep strength and low creep ductility, and the later is associated with grain boundary liquation (**11, 12**).

One important Nickel-based superalloy, presently used in many industrial gas turbines, is IN-738LC . This material can operate for more than 100,000 hours at levels of stress and temperature above 138 MPa and 1103 K (**13**), respectively. IN-

738LC was designed with a relatively high chromium content for corrosion resistance and low density for reduced weight; therefore, it is mainly intended for use in rotor blades, which are exposed directly to the hot gases and subjected to stresses from centrifugal forces (**2**).

Since the extent of weld repairs on gas turbine rotating blades is basically limited to low stress areas, there is then the need for studying the metallurgical response of superalloy IN-738LC to the laser beam welding process, and explore the possibility of obtaining sound weld deposits with metallurgical characteristics equivalent to the finished superalloy cast components. Extending material build-up to high stress areas will allow the recovery of blades that are deemed as scrap by present repair limit criteria.

1.2- **SCOPE**

The published literature presents several papers on the weldability of superalloys by high energy beam processes (**14, 15, 16**), including parametric studies that look at correlation between beam power, welding speed, penetration and weld bead geometry. There are also several papers that report the relation between welding parameters and microfissuring in the heat affected zone (**5, 6, 7, 17**). However, little work is available on the effects of the laser beam welding process on the microstructure of the weld deposits. Therefore, the proposed research will focus on studying the compositional and microstructural effects of the laser beam welding process on a particular superalloy (IN-738LC). The hardenability, rather than the study of parametric correlations, is used as an evaluative criteria.

CHAPTER 2

REVIEW OF RELATED LITERATURE

2.1- SUPERALLOYS

2.1.1- Service Requirements for Superalloys

In a broad sense, superalloys are complex solid solution hardened alloys, usually fcc, further strengthened by a precipitation hardening mechanism. Due to their high strength and oxidation resistance, they are generally used in elevated temperature applications.

During the early stages of superalloy development (1940's to 1960's) emphasis was placed on optimizing the chemical composition to obtain maximum solid solution hardening, and applying simple age hardening treatments which allowed engine firing temperatures of 1030 K. But the need for higher engine outputs, thrust and thermodynamic efficiency has required for the materials to be used at higher temperatures (**18**). An increase of 70 K can provide corresponding increases of 10 to 13% in output and 2 to 4% in efficiency, with a significant cost benefit (**13**). By 1992 the fuel efficiency of industrial gas turbines had surpassed the 50% mark, due to the high firing temperatures accomplished.

For the materials to keep pace with the higher temperature requirements, complex casting and forging practices, as well as heat treatments have been used to activate all possible strengthening mechanisms. The objective of superalloy design consequently has been to obtain a proper balance between intergranular and grain boundary strengths, with the tendency to eliminate grain boundaries.

Material service requirements in gas turbine engines are generally centered on:

- Creep strength
- Tensile strength
- Low and high cycle fatigue
- Cyclic rupture (creep-fatigue interaction)
- High temperature oxidation and corrosion

To comply with these requirements, the alloy designers make use of different strengthening mechanisms that affect the matrix and precipitates, as well as the grain boundaries, grain size and grain orientation. Additionally, oxide dispersoids are added in some alloys to obtain additional strength at temperatures above 85% of the melting point (**19**).

2.1.2- **Metallurgy of Superalloys**

Nickel base superalloys are materials based in the Ni-Al binary system, composed of γ (gamma) and γ' (gamma-prime) phases. The γ phase is fcc Ni or Ni-Al solid solution and γ' has ordered fcc structure (Ll_2), often expressed as Ni_3Al, where Ni atoms are placed at the center of the unit cell and Al atoms are at the corners. The dispersed intermetallic γ' precipitates are coherent with the matrix, with a lattice mismatch between 0 and 0.5% .

The γ Matrix

Even though Ni does not have one of the highest values of modulus of elasticity or one of the lowest values of difussivity, which are the basic requirements for creep resistance, it has excellent resistance to severe temperatures in air atmospheres. For example, Ni-base alloys can be used at temperatures of 0.9 Tm for times up to 100,000 hours. The reason for this endurance is attributed to (**20**):

1. High phase stability in the alloyed condition due to its nearly filled 3d electron shell.
2. The tendency, with chromium addition, to form a Cr_2O_3 rich protective film, which restricts the diffusion rate of metallic element outward and oxygen and sulfur inward.

The tendency, with aluminum addition, to form alumina scales which are highly oxidation resistant.

The matrix can be solid solution strengthened by Co, Fe, Cr, Mo, W, Va, Ti and Al, which differ from Ni by 1 to 13% in atomic diameter, so that hardening can be related to solute diameter mismatch. An additional hardening effect is due to short range ordering, which has been observed in Ni alloys with 20-25% Cr. Consequently, solute elements can restrict the mobility of dislocations by lattice expansion and/or short range ordering (**20**).

According to the relative effect of these mechanisms, it has been found that Al, W, Mo and Cr contribute strongly to strengthening, while Fe, Ti, Co and Va are only weak solid solution strengtheners.

At temperatures above 0.6 Tm, which is the range of high temperature creep, γ strengthening is diffusion dependent, and the heavy elements Mo and W become most useful, whereas the effect of the other elements vanish.

The γ' Precipitate

To provide strength at high temperatures, it is necessary to use another mechanism, namely, precipitation hardening. The high Ni matrices (above 25% Ni) offer the unique possibility of precipitating the γ' phase, and at the same time limiting the possibility of precipitating more complex, undesirable phases. This is because the

undesirable phases produce lattice size changes, and the Ni atom lacks compressibility due to its third electron-shell state (**21**).

The γ' is a type A_3B compound, where a relatively electronegative element such as Ni or Co is the A and a more electropositive element such as Al, Ti or Nb is the B; therefore, it is commonly denoted as $(Ni,Co)_3(Al, Ti, Nb)$. This phase can precipitate as spheres, cubes or plates depending on the extent of lattice mismatch. The spheres are stable between 0-0.2%, the cubes between 0.5-1% and the plates above 1.25% lattice mismatch.

The γ' phase presents the following important characteristics:

- It has a compatible structure (fcc) and lattice constant (around 1% mismatch) with respect to the γ matrix, which allows homogeneous nucleation with low surface energy and long time stability.
- It presents an ordered structure (Ll_2), which contributes with anti-phase boundary (APB) strengthening.
- Its strength increases with temperature, which is believed to be due to a change in degree of order with temperature. Additionally, its inherent ductility prevents embrittlement even if it precipitates at grain boundaries.

Cr, Fe and Co have an important effect on γ' as they lower the solubility of Al and Ti in the matrix, and therefore promote its precipitation. Thus, these elements are used to increase the volume percentage of the precipitate. This is important since it has been found that an increase from 14 to 60% γ' can quadruple the strength of superalloys (**20**).

In general, the level of strengthening offered by γ' to the Ni-base alloys can be related to the following factors: ordering, anti-phase boundary and coherence strains (related to morphology of the precipitates). Therefore, in order to maximize the interaction between the γ' particles and the dislocations, it is necessary to control the

size, shape, amount and distribution of the γ'. From a study of the relation between the mean particle diameter and the hardness of Ni-base superalloys (**20, 22**), it has been found that for most alloy compositions, the highest hardness is achieved for a size between 0.1 and 0.5 μm. Furthermore, a study of the relation between the volume percentage of γ' and the rupture strength of the material has shown that the high temperature strength increases as the amount of γ' present is increased. Therefore, it is important to control the precipitation and aging of this phase to obtain a microstructure that causes the greatest dislocation pinning.

Carbides

As temperatures increase above 0.6 Tm, the hardening effect of the γ' is diminished and creep phenomenon starts taking place. Creep damage consists of nucleation, growth and coalescence of grain boundary cavities, forming intergranular microcracks that lead to the sliding or migration of adjacent grains and ultimate fracture. One way to control this phenomenon is to form discrete, also called serrated, carbides along the grain boundaries. On the other hand, continuous bands of carbides at grain boundaries make the alloys susceptible to creep damage (**21**). Additionally to influence the rupture strength at high temperature, carbide morphology also affects the low temperature ductility. Furthermore, the formation of carbides can influence the chemical stability of the matrix through the removal of reacting elements.

The common carbides present in Ni-base superalloys are MC, $M_{23}C_6$ and M_6C. MC carbides, which form during freezing, usually take a random cubic or script morphology, and are distributed heterogeneously throughout the alloy at intergranular and transgranular positions. The metallic elements typically associated with this type of carbide are: Hf, Ta, Nb and Ti, and they can substitute for each other. The MC, single monatomic fcc carbide, found in most cast and wrought superalloys, can readily decompose into $M_{23}C_6$ and M_6C-type carbides during heat treatment or service.

However, additions of Nb and Ta tend to counteract this effect, producing MC carbides that do not break easily even during solution treatment.

$M_{23}C_6$ carbides form from degeneration of MC carbides and from soluble carbon residual in the alloy matrix during low temperature heat treating and during service (1030 - 1255 K). They show a marked tendency to form at grain boundaries as irregular, discontinuous blocky particles. These carbides have a complex cubic structure, which approximates the composition $Cr_{21}(Mo,W)_2C_6$ when Mo and W are present. Also, Ni, Co and Fe can substitute for Cr. $M_{23}C_6$-type carbide has a significant effect on rupture strength, apparently through inhibition of grain boundary sliding when precipitated as discreet particles.

M_6C-type carbide also forms during heat treating and service, but generally at slightly higher temperatures than $M_{23}C_6$-type carbides (1090-1255 K). They have a complex cubic structure with a widely varying composition (M_3C to $M_{13}C$), that depends on alloy content of the matrix. M_6C-type carbides typically form when the Mo and/or W content is high (more than 6-8 atomic %). It is mainly beneficial as a grain boundary precipitate to control grain size in processing wrought alloys.

The decomposition of MC-type carbide into $M_{23}C_6$ and M_6C that occurs during heat treatment or service yields carbon, which permeates the matrix and triggers further reactions, and the most beneficial decomposition reaction is considered to be:

$$MC + \gamma \rightarrow M_{23}C_6 + \gamma'$$

This reaction yields a blocky carbide surrounded by γ' at the grain boundaries, forming a relatively ductile, creep resistant layer. In addition to the effect on grain boundaries, uniform inner grain distribution of MC and M_6C carbides offers strength to the alloy up to 0.8 Tm.

Grain Size and Orientation

Since the most demanding service conditions correspond to the rotating parts, where cyclic stresses are present, fatigue is also an important consideration in superalloys.

In order to improve fatigue resistance, thermomechanical treatments are selected so that a controlled amount of grain growth is produced. Basically, the solution temperature is selected so that partial or full γ' dissolution takes place, but a particular type of carbide, (Ti, Mo)C , stays present. This type of particle is used to pin the grain boundaries during subsequent heat treatments.

The grain structure not only affects the fatigue resistance, but also the strength of superalloys. However, contrary to fatigue life, rupture life and creep resistance increase with grain size. Therefore, a balance must be set to avoid excessively fine grains which decrease creep and rupture strength, or large grains which lowers fatigue resistance as well as tensile strength.

The fine grain size has the following effects (**23**):

- Improves high cycle fatigue over the entire temperature range
- Improves low cycle fatigue up to approximately 780 K
- Improves UTS and YS up to 920 K
- Improves creep strength up to approximately 870 K
- Reduces creep strength above 980 K

Further improvements in mechanical properties can be achieved by controlling the orientation of the grains and their boundaries. By using directional solidification or single crystal growth which aligns the slip planes in the most favorable conditions, the yield strength can be significantly improved. Directional solidification also increases the ductility, and the absence of weak, transverse grain boundaries produces an

extended tertiary creep life. An additional benefit is the greater difficulty of crack initiation and propagation obtained by the lack of grain boundaries in the maximum tensile direction (**20**).

Finally, with the introduction of a directionally solidified structure, grain boundary ductilizers and strengtheners such as B, Zr and Hf can be removed. Since these elements significantly reduce the melting point of the alloy, their elimination results in a 28 to 56 K (50 to 100 °F) improvement in strength capability (**21**).

2.1.3- **Phase Stability**

As it was mentioned before, the thermomechanical treatments applied to the superalloys are designed to give a proper balance between intergranular and grain boundary strength. Inside the grains, this is achieved by providing solid solution strengthening of the matrix and controlling the size, shape, distribution and amount of the phases present (γ', carbides and dispersoids). The grain boundary strength is achieved by proper distribution of carbides and the presence of a γ' envelope. Similarly, fatigue and creep strength are obtained by controlling the size and orientation of the grains. However, fusion of the base material during welding replaces the standard equilibrium and distribution of phases obtained by thermomechanical and heat treatments by a cast structure. In the same manner, the high temperatures reached in the HAZ trigger diffusion mechanisms that cause instabilities of the microstructure. The result may be the dissolution or the coarsening and agglomeration of the γ'; the degeneration of the MC carbides, which can form additional grain boundary $M_{23}C_6$ precipitates; and the possible formation of new phases. All of these phase changes affect the strength of the material.

If the thermal exposure exceeds about 0.6 Tm (**21**), the γ' ripens (increase in size) at a significant rate, facilitating dislocation bypassing. The coarsening of the γ'

precipitates occurs by an Ostwald ripening mechanism (exponential function) in which the larger particles grow at the expense of the smaller ones.

Exposure to high temperatures may also transform γ' to other Ni_3X compounds such as Ni_3Ti (eta phase "η") or Ni_3(Nb, Ta), which can be detrimental to stress rupture strength. To retard this transformation, trace levels of boron are commonly added to commercial alloys. Equilibrium segregation of boron to grain boundaries retard nucleation of Ni_3X cells.

The most effective ways of extending the stability of γ' at high temperatures are (**20**):

- Decrease coherence strains by increasing the Cr content and lowering the Ti/Al ratio
- Increase the volume percentage of γ'
- Add elements such as Nb and Ti (from 2 to 5 wt %) which partition to γ' and cause slow diffusion

In the case of the carbides, to diminish the coarsening process as temperature is increased, the elements B, Zr and Mg are added to the alloy . These elements segregate to the grain boundaries because of their larger size (21 to 29% over and under Ni), and consequently, retard diffusion.

When composition has not been carefully controlled (excessive amounts of Co, W, Mo, Ta and Cr), undesirable phases can precipitate during high temperature exposure (**21**). These phases, called topologically closed packed (TCP), may appear as thin linear plates, often nucleating on grain boundary carbides. The most common TCP phases found in Ni superalloys are σ and μ phases. By providing an excellent source for crack initiation and propagation, σ phase can reduce low temperature ductility as well as high temperature rupture life. To minimize the possibility of formation of TCP phases, strict control of the chemical composition is required.

The changes in the γ' phase are closely related to loss of tensile strength and creep strength, while the changes in the carbides and the precipitation of new phases (topologically closed pack) are related to loss of tensile ductility, creep ductility, rupture strength, impact toughness and thermal fatigue (**24**).

2.1.4- **Superalloy IN-738 / IN-738LC**

Superalloy IN-738 is a heat treatable Ni-Cr-Co base casting alloy, which provides a high creep-rupture strength up to 1270 K. It was designed with a high chromium content to provide a corrosion resistance, superior to that of most other casting alloys for high temperature service. Consequently, it is used in the high pressure stage blades and vanes of land based gas turbines (**25**). Table 1 shows its nominal chemical composition and mechanical properties. The modified version of the alloy, designated IN-738LC, has lower carbon and zirconium contents for improved castability. This modification has no significant effects on the mechanical properties.

The high strength of IN-738LC is the result of solid solution strengthening from chromium, molybdenum, tungsten and cobalt; precipitation hardening from a γ' phase consisting of nickel-aluminum-titanium compounds; and grain boundary strengthening from MC and $M_{23}C_6$ carbides (**26**).

IN-738LC is normally vacuum melted and vacuum investment cast, where it is subjected to the formation of microporosity during solidification, which reduces its mechanical properties. Since this condition can be minimized, but not always prevented by good foundry practice, hot isostatic pressing is used to at least partially eliminate the detrimental effect of microporosity.

TABLE 1- CHEMICAL COMPOSITION AND MECHANICAL PROPERTIES OF ALLOY IN-738/IN-738LC (COMMERCIAL SPECIFICATION)

ELEMENT	IN-738 (wt %)	IN-738LC (wt %)
C	0.15-0.20	0.09-0.13
Co	8.00-9.00	8.00-9.00
Cr	15.70-16.30	15.70-16.30
Mo	1.50-2.00	1.50-2.00
W	2.40-2.80	2.40-2.80
Ta	1.50-2.00	1.50-2.00
Nb	0.60-1.10	0.60-1.10
Al	3.20-3.70	3.20-3.70
Ti	3.20-3.70	3.20-3.70
B	0.005-0.015	0.007-0.012
Zr	0.05-0.15	0.03-0.08
Fe	0.50 max	0.50 max
Mn	0.20 max	0.20 max
Si	0.30 max	0.30 max
S	0.015 max	0.015 max
Ni	Balance	Balance

TENSILE PROPERTY	ROOM TEMP.	HIGH TEMP (922 K)
UTS	793 MPa	793 MPa
YS (0.2%)	690 MPa	586 MPa
Elong.(min.)	4.0 %	4.0 %
Red. Area (min.)	5.0 %	5.0 %

STRESS RUPTURE PROPERTY (1255 K / 151.69 MPa)	
Life (min)	30 h
Elongation (min.)	5.0 %
Red. of Area (min.)	5.0%

Additionally, this alloy is used in the precipitation-hardened condition; for which the following thermomechanical-mechanical and heat treatment cycles are used (27):

- HIP at 103 MPa (15000 psi) and 1473 K (1200 °C) for 4 h
- Solutionize at 1393 K (1120 °C) for 2 h and air cool
- Precipitation hardening at 1118 K (845 °C) for 24 h and air cool

The microstructure of IN-738LC in the as cast condition presents a wide range of precipitate sizes and morphologies. However, the above heat treatment has a homogenizing effect on the precipitate distribution, although variations still exist between interdendritic and dendritic core regions. In the fully heat treated (FHT) condition, the γ' phase comprises essentially a bimodal distribution of primary cuboidal precipitates of approximately mean diagonal 0.5 μm, together with secondary spheroidal precipitates of approximately mean diameter 0.1 μm **(25, 28)** Additionally, isolated areas of large blocky γ-γ' precipitates, resulting from eutectic reaction, can also be present. The maximum γ' volume fraction attainable by the material is about 0.45 **(10)**. The MC carbides, either in chinese script or blocky morphology, occupy intragranular and intergranular sites, with a higher volume fraction in the interdendritic regions. The $M_{23}C_6$ carbides occur as a grain boundary precipitate.

2.2- THE LASER BEAM WELDING PROCESS

2.2.1- Laser Processing Principles

Laser Beam Generation

The "Laser", which is an acronym for Light Amplification by Stimulated Emission of Radiation, is a devise that generates a concentrated, coherent light-beam in the wavelength range covering the near ultraviolet, visible and infrared regions **(9)**.

The emission device is based on an optical resonator that consists of a system of mirrors arranged such that the effective length of a stimulated laser medium is

increased by multiple reflections. In simple terms, the laser beam is generated when a laser medium is stimulated by bursts of white light, electric discharge, chemical reaction or other means, which produces a light beam of enormous power that bounces back and forth between two mirrors. The beam increases in strength each time it passes through the medium, and because one of the mirrors is partially transparent, an intense parallel shaft of light is obtained from the device (**30**).

There are basically two types of laser media used in industrial devices: solid-state neodymium-doped yttrium-aluminum-garnet (Nd-YAG) and molecular carbon dioxide. Other solid, liquid and gaseous laser sources, such as Nd-doped glass, ruby, dye-rhodamine 6 and argon-ion, have also been developed, but they have shown to be less efficient and unstable, and have lower output power (**31**).

Solid state YAG lasers use a host medium that holds implanted Nd^{3+} ions. The ions form the lasing medium, called lasant, which actually emits the light when exited in the host material. This type of laser can yield an average power of 50 to 500 W for the continuous mode, and 10^7 W or more for the pulse mode. However, those outputs are low as compared with gas lasers, because of the small linear dimensions of the synthetic crystals and their low thermal conductivity, which causes difficulties in cooling the lasing element.

CO_2 lasers can generate very high average powers ($>$ 15 KW) in continuous-wave and repetitive-pulse modes. The working medium in a gas laser can be a pure gas, a mixture of gases or a mixture of gas and metal vapor. The excitation of the gas is obtained by an electrical discharge, a chemical reaction or an adiabatic outflow of the heated gas through a supersonic nozzle. Of these, gas-discharge lasers are more extensively used in industry.

In CO_2 lasers, the lower vibrational levels of exited CO_2 molecules generate infrared radiation at a wavelength of 10.6 μm. Nitrogen and helium are added to the

CO_2 gas; the former intensifies the lasing actions and the later increases the heat conduction of the mixture, speeding up heat removal, and thereby reducing medium temperature.

The coherent radiation produced by the optical resonator can be concentrated to an extremely small spot, comparable in area to the square of the wavelength. This is accomplished by a beam focusing and control optical system, composed of mirrors and lenses which enhances the efficiency and position of the beam with respect to the target.

Metal-Laser Beam Interaction

Laser beam processing consists of photon energy transfer to a material. A photon is an elementary energy particle regarded as massless with an energy $h\nu$, where h is Planck's constant and ν is the equivalent frequency. The equivalent wavelength of the photon, λ, is given by C/ν, where C is the speed of light.

The energy of an irradiated photon in a laser beam is in the range 0.1 to 10 eV. When projected onto a surface of a metal, part of this photon energy is transmitted as thermal vibration energy to the outer-shell or conduction electrons in a metal surface layer 0.1 to 1.0 μm thick. The vibration energy is then conducted to the surrounding areas as heat by collision of electrons. The other part of the incident photon energy is reflected from the target surface.

Since most of the laser induced heat propagates into the bulk metal by way of electron conduction, the laser-induced thermal processes are similar in nature to conventional processes of metal heating, and the heat transfer can be dealt with on the basis of classical heat conduction theory.

It has been found that nearly all materials can be melted and vaporized by laser-beam irradiation, including high heat-resistant ceramics, so that it has the ability to thermally process all kinds of materials.

The efficiency with which a material absorbs the laser radiation is defined as the material's absorbance, and it varies with the wavelength of radiation. For a CO_2 laser beam (λ = 10.6 μm) with an angle of incidence of 90°, the ideal absorbance for most metals varies from 1.1 to 8.0 %. For a Nd-YAG laser beam (λ = 1.064 μm) with the same incident angle, the ideal absorbance varies from 3.6 to 43%. Therefore, metals most heavily reflect CO_2 laser beams.

The above ideal values can increase significantly with changes in the surface finish or chemical composition of the target. For example, an increase in surface roughness, R_Z , from 34 to 120 μm on a stainless steel surface, raises the absorbance by a factor of 1.2 to 1.5, whereas a metal powder coating or a paint coating give a 2.0 to 2.5 fold increase (**12**).

2.2.2- **Laser Beam Welding**

Process Characteristics

The possibility of generating light of narrow spectrum band width, of uniform phase and with a parallel beam, that delivers a power density greater than 10^2 W/mm^2 , is what allows the potential for the laser beam welding processing of metals (**31**). The only other intense energy process that approaches the characteristics of laser welding is electron beam process; however, it requires a high vacuum in the processing chamber in order to obtain proper fusion control. In contrast, laser welding is less environmentally sensitive and can be performed at atmospheric pressure in air or in

shielding gases such as argon, helium or carbon dioxide. The process is easily controlled by adjusting the beam parameters. Also, unlike electron beam and arc welding, the laser beam is not affected by magnetic fields, so it yields a high quality weld deposit on sensitive materials.

Because of the high energy density obtained with both continuous and pulse modes, the bulk of molten metal and the HAZ are small and the process speed can be very high. Additionally, the low heat input results in very slight distortion of the deposit.

The power density of laser beams can reach such magnitudes, that it is actually limited to a threshold power density, q_{th}, above which the metal vigorously vaporizes, so that metal ejection from the weld pool impairs the process. In practice, fusion is carried out in the range from 10 to 10^3 W/mm^2. Power densities below 10 W/mm^2 are insufficient to provide quality weld deposits (**9**).

Three definite combinations of power densities, q, and interaction or dwell time, t, are applicable in laser fusion:

1. $q = 10$ to 10^2 W/mm^2 and $t > 10^{-2}$ s. This corresponds to continuous laser welding, where varying q and t in the specified limit allows fusion of most materials in a wide range of thicknesses.

2. $q = 10^2$ to 10^3 W/mm^2 and $t > 10^{-3}$ s. This is specific to pulse processing with frequencies in tens to hundreds of Hz. It can yield welds in a wide range of depths and requires a lower heat input than continuous laser processing.

3. $q = 10$ to 10^2 W/mm^2 and $10^{-3} < t < 10^{-2}$ s. This corresponds to a similar interaction time but a larger pulse length than in the second case. It is used for spot welds of small depth.

Power densities in the range given above (10 to 10^3 W/mm^2) can give rise to two different fusion modes: conduction and deep penetration. In the conduction mode, the temperature gradients of the order of 10^5 K/mm produced in the substrate originate surface-tension-driven thermocapillarity flow in a weld pool, with surface velocities of around 1 m/s. This convection effect determines the pool shape, aspect ratio and surface ripples, and can account for defects such as variable penetration, porosity and lack of fusion. It also controls the pool mixing and therefore, affects the composition of the deposit.

In deep penetration mode, a keyhole is produced when a beam of sufficient high power density causes vaporization of the substrate and the vapor pressure in the crater causes an upward displacement of the molten metal along the walls of the hole. The hole acts as a blackbody, adding in the absorption of heat deep in the material. A steady state is formed when the continuously generated vapor counteracts the effect of the flow of the liquid and the surface tension, which tends to obliterate the cavity. The material lost by vaporization, which may change the chemical composition, may result in a depression at the top of the deposit, in porosity as an inward deformation of the work piece, or in a combination of these.

Laser Welding Parameters

The most relevant independent process parameters are laser-beam power, laser-beam diameter, focal position, depth of focus, absorbance, shielding gas and traverse speed. The incident beam power and beam diameter define the power density, which is directly related to depth of penetration. The important dependent parameters are pool geometry, microstructure and mechanical properties (**32**).

Because of the nature of the beam, laser-beam diameter is difficult to measure for high power beams. One definition establishes that Gaussean beam diameter, d_G, is the diameter where the power has dropped to $1/e^2$ or $1/e$ of the central value. The $1/e^2$

measurement contains almost 86% of the total power, whereas 1/e contains slightly over 60%. The diffraction limited focal spot size, d_{mean}, defines the ideal focus beam diameter for TEM_{00} mode, which is given by 1.27 x f x λ / D, where f is the focal length of the focusing optics, λ is the wavelength of the laser beam and D is the unfocused beam diameter. The actual value is larger due to aberrations and other imperfections of the focusing optics.

Besides its diameter, another important characteristics of a laser beam is its spatial distribution. Every laser resonator has certain stable configuration of the electromagnetic field called modes, which defines the spatial distribution. By convention, the modes are indexed as TEM_{mn}, meaning a transverse electromagnetic mode with m number of radial zero fields and n number of angular zero fields. TEM_{00}, offered by most of the fast axial flow lasers, corresponds to the ideal Gaussean beam that provides the smallest focus spot and the highest power density. TEM_{01}, offered by most of the transverse flow lasers, corresponds to a doughnut-shaped spatial distribution.

Another important parameter is the position of focus with respect to the substrate surface, which affects the weld pool profile and penetration. It has been reported that the optimum position of the focus for autogenous conventional welding is 1.25 mm to 2.5 mm below the surface, depending on the thickness of the work piece and the laser power used (**12**). If the focal point is positioned deeper inside the work piece, a "V" shaped weld results, which requires more precise alignment and melts more base metal than a parallel-sided weld. If the beam focus is positioned above the surface of the work piece, a large "nail head" with a consequent low surface profile results. The addition of filler material, such as metal powder, changes the behavior of the weld pool, and the position of focus is selected according to the feed design.

Depth of focus, Z, defined as the distance over which the focus beam has the same approximate intensity, is an important parameter when welding substrates that

may distort thermally, such as thin section parts, and when building up surface layers, such as deposition welding. Quantitatively, it has been defined as the range over which the focused spot radius is increased by 5%. The depth of focus is proportional to the f x λ of the optics. Increasing this parameter, increases the beam diameter and decreases the power density; therefore, the parameters must be optimized for each particular application.

As it was mentioned before, absorbance defines the fraction of the laser energy absorbed by the substrate. Since the infrared absorption of metals largely depends on the conductivity by free electrons, absorbance is a function of the electrical resistivity of the substrate. However, normally it is not possible to modify this property of the base metal. Besides using coatings or increasing the roughness of the surface, the absorbance can be increased by the use of powder filler metal instead of wire-fed filler metal. Wire surfaces reflect a considerable amount of energy, reducing the efficiency of the process (**33**).

The addition of reacting gases, such as 10% O_2 to an argon shielding gas, has shown also a positive effect on absorbance, increasing the welding depth up to 10%. Another way of increasing the absorbance is by keyhole formation, which provides efficient welding of even highly reflective materials such as aluminum.

The shielding gas, used to protect the weld surface from oxidation, has an important effect on the welding characteristics as it may produce a plasma that absorbs and scatters the laser beam. The higher the power, the higher the interaction with the plasma. Therefore, it is necessary to remove or suppress the plasma, which can be attained by selecting a proper gas mixture.

The gases that allow greater penetration do not necessarily provide the best displacement of air from above the weld, and hence, the best oxidation protection. Thus, compromises are established to obtain the best quality deposit. Helium has been

found to improve beam transmission, whereas argon can cause severe beam blockage. It has also been observed that additions of hydrogen, sulfur hexafluoride and CO_2 to helium enhances penetration. The gases that have the higher ionization potential and minimize the formation of plasma also have low atomic number and low mass, and therefore, are not very effective in displacing the air in a short time. The best result is then obtained by a mixture of heavier and lighter gases, such as 10% Ar-90% He.

Finally, the traverse speed is the parameter used along with the beam diameter to set the dwell time. By decreasing the traverse speed and consequently increasing the dwell time, the penetration depth is increased. However, the size of the fusion zone (nugget) is also increased, which may have a negative effect on the strength of the joint. Typically, for a given thickness and power, a particular speed is selected to deliver a nugget size specified by the design.

2.3- WELDING OF SUPERALLOYS

2.3.1- Weldability of Superalloys

Welding is one of the main fabrication and repair techniques used for superalloy components; however, new alloys have been traditionally developed on the basis of high temperature strength, stress rupture and oxidation properties, and welding has only been considered later in the application stage of the alloys. This has resulted in unpredictable and uncontrolled metallurgical variations, causing problems such as high susceptibility to cracking (**21**).

Fusion welding disrupts the very specialized element and phase distribution that is responsible for the strength properties of the alloy, and replaces the original microstructure by a cast structure or fusion zone and a heat affected zone.

Fusion Zone Effects

The microstructure formed in the fusion zone of the weld is largely dominated by two interrelated occurrences: elemental segregation and dendrite formation (**5**). At the fast cooling rates that take place during welding, the phenomenon of segregation during non-equilibrium solidification occurs. If the equilibrium partition coefficient (concentration in solid over concentration in liquid) is less than unity, the solid will have less solute than the liquid when freezing, causing enrichment of the liquid. This results in a lowering of the freezing temperatures as the remaining liquid is enriched. Hence, a liquid that would freeze at relatively high temperature under equilibrium conditions could, by solute segregation during rapid freezing, have liquid remaining to much lower temperatures (depression of solidus). By this mechanism, the dendritic solidification that takes place in the fusion zone produces a repetitive microstructure morphology with enriched interdendritic spaces and depleted dendritic cores.

Several studies have shown that in precipitation hardening superalloys, hardening elements such as W, Nb and Al segregate, causing inhomogeneous precipitation during the post-weld heat treatments intended to restore the mechanical properties (**5**). A measure of segregation is given by the solidification distribution coefficient, k, which is the ratio of dendritic core element concentration to the bulk element concentration. For example, a typical value of Nb segregation in Ni-base superalloy Custom Age 625 Plus* is 1.80 wt % in dendrite core, compared to 3.40 wt % nominal alloy concentration, giving a k value of 0.53 (**34**). Additionally to depleting some areas of the strengthening elements, segregation can also affect the oxidation resistance by reducing the concentration of elements such as Cr and Al in some local regions of the surface.

The depression of solidus during solidification, besides causing segregation, may also tie up the hardening elements in non-equilibrium intermetallic brittle phases

* Custom Age 625 Plus is a registered trademark of Carpenter Technology Corp.

such as Laves phase. These non-equilibrium phases form either at the termination of solidification or upon cooling of the weld metal to ambient temperature (**34**). Therefore, the ductility of the weld is always reduced, which may lead to cracking.

Heat Affected Zone Effects

The metallurgical changes that occur in the HAZ are also of considerable importance. The main concern in this case is the phenomenon of constitutional liquation, by which localized melting can occur.

In the case of a simple binary system, constitutional liquation takes place when the alloy is heated at such a rate that a susceptible phase cannot dissolve before the alloy reaches a local system solidus. Therefore, melting invariably occurs at the interface between the precipitate and the matrix, where a local equilibrium prevails. This liquation can occur below the overall solidus of the alloy, and thus be located in the HAZ away from the fusion zone (**12**).

Regions in the HAZ that are exposed to high temperatures can also undergo exaggerated grain growth, solutioning and precipitation of carbides or γ', as well as ripening. These changes may cause deterioration of properties. However, these degradation processes are diffusion dependent and require time. High heat imput processes such as Shielded-Metal Arc, Gas-Tungsten Arc and Gas-Metal Arc produce slow thermal cycles that promote these changes. Low heat impute processes such as Laser Beam Welding, on the other hand, produce fast cycles that minimize the diffusion process around the fusion zone.

2.3.2- **Welding Discontinuities**

The weldability of superalloys is mainly affected by cracking at the HAZ; however, other discontinuities such as porosity and undercut can also occur in the fusion zone.

Cracking Mechanisms

Cracking occurs when an imposed strain exceeds the ability of the material to deform. If a material can undergo 10% elongation, it will only crack under a strain in excess of 10%. Based on the coefficient of thermal expansion, Young's Modulus and a welding thermal cycle, it has been calculated that the maximum uniform strain than can be developed during welding is on the order of 0.1 % (**21**). Greater strains can occur only over macro-regions associated with areas of reduced section or because of thermal and yield strength gradients, which produces a strain-concentrating effect. However, strains will not develop to any significant magnitude within micro-regions. Hence, strains no larger than 1 % are expected in a weld HAZ. This observation allows the establishment of a criterion for predicting HAZ cracking, by assuming that this defect will only occur when the alloy is in a condition of zero or near zero ductility.

Conditions of very low ductility associated with welding of precipitation hardened Ni-base superalloys are related to two factors: age hardening through precipitation of γ' which originates strain age cracking, and constitutional liquation which originates from liquation cracking.

Strain-Age Cracking

In order to weld in a condition of high ductility, the process is usually carried out after the material has been solutioned, and the maximum strength is recovered afterwards by a resolution anneal and aging heat treatments. However, the welding process invariably produces a HAZ thermal cycle which may dissolve the over aged γ' at a particular distance of the weld pool. During cooling after welding or during re-heating in subsequent treatments, the γ' reprecipitates in these areas, producing a region of higher creep strength and low creep ductility.

The residual stresses are normally relieved by a process of creep and plastic deformation; however, the reprecipitated areas in the HAZ may be strengthened and embrittled to a point that it is not capable of relieving the stresses producing cracking at the grain boundaries in the HAZ. Imposed stresses, produced by constraints in the weld, add to the residual stresses that increase the susceptibility to cracking.

This phenomenon, called strain-age cracking, depends on both the rate and magnitude of γ' precipitation, which is a function of the Ti + Al content (**21**). An empirical relationship indicates that those alloys that exceed a combined Ti + Al content of 6 % have a high susceptibility to strain-age cracking. IN-738LC has a combined Ti + Al content of 7.4 %, which indicates that it would be a difficult to weld material. The Laser Beam Welding process produces a narrower HAZ than the standard processes which decreases the possibility of occurrence of this phenomenon. However, the high cooling rates produce higher localized residual stresses, which promote the formation of cracking.

Liquation Cracking

This type of cracking results from the formation of a liquid film at the grain boundaries adjacent to the fusion boundary due to constitutional liquation, and the inability of this film to accommodate thermally induced tensile stresses during weld cooling (**11**). This phase transformation is considered to be transient in nature and dependent on diffusion. If there was enough time for diffusion to homogenize the alloy, the melting point of the homogeneous composition will be higher than the local temperature, causing the solidification of the liquid phase (**35, 36**)

Constitutional liquation can result from two factors (**12, 35**):

1. A rapid heating rate that takes a normally low temperature phase above its equilibrium stability temperature.

2. Coring type segregation during casting, which causes the system to create non-equilibrium phases such as Laves phases, or an over-abundance of an equilibrium phase such as MC carbides. Both the non-equilibrium phase and the excessive fraction of equilibrium phase can constitutionally liquate.

It has been observed that the niobium-rich carbide is typically associated with grain boundary liquation (**11**). Since alloy IN-738LC contains Nb as a hardening element, it may precipitate niobium containing carbides. Additionally, the liquation of Laves phases, $(Ni, Cr, Fe)_2(Nb, Mo, Ti)$, has also been found to play an important role in microcracking susceptibility (**17**). This intermetallic phase precipitates in some of the Ni-base superalloys, given the proper segregational composition.

Impurities such as S, P, B and Cu have also been observed to affect liquation cracking (**37, 38, 49, 40**). They can increase the susceptibility to cracking by increasing the wetting of the intergranular liquid, depressing the solidus temperature, forming low-melting-point precipitates and increasing the amount of liquid present on the grain boundaries.

Besides chemical composition, microstructural characteristics such as grain size also affect liquation cracking. When the HAZ begins to accumulate strain from residual stresses, grain boundary sliding operates to accommodate that strain. However, a large grain size does not accommodate the strain as readily as smaller grain size, and the potential for crack initiation at grain boundary triple points, and therefore liquation cracking, is increased.

If the melting of the susceptible phase is accompanied by sufficient thermal stress, cracks can form along the HAZ grain boundaries and extend into the base metal. If the liquation line is open to the fusion zone, the fusion zone can act as a source of liquid to backfill and heal the cracks than might form. Therefore, liquation cracks can only initiate in the HAZ and not at the fusion zone.

The microfissuring that occurs in the HAZ of superalloys requires then a combination of three main conditions to cause failure (17):

1. A level of stress that initiates cracking.
2. A crack susceptible microstructure that contains one or several of: low melting point grain boundary phases, liquatable primary phase, large grain size and/or elemental segregation.
3. The ability of liquid grain boundary phases to wet grain boundaries.

To reduce the possibility of liquation cracking, the following metallurgical factors must be taken into account:

1. Grain size should be minimized
2. MC carbides should be used to control grain size, since they decrease liquid penetration due to the fact that their liquation temperature is close to the system melting temperature.
3. The amount of the precipitate that liquates should be minimized. If this is not possible, an increase in the amount of precipitate may produce enough liquation to initiate backfilling from the fusion zone and promote filling of cracks.
4. Impurity content should be kept to a minimum.
5. Segregation should be decreased by applying some combination of solution and homogenization heat treatment, followed by rapid cooling.

Other Discontinuities

Besides cracking, laser beam welding has been found to produce some particular defects which are also common to other high energy processes, such as electron beam and plasma arc welding.

Porosity is a common occurrence, especially when using deep penetration in the pulsed beam mode. During the beam-off portion of the cycle, the pressure produced by vaporization inside the keyhole decreases to a point that it can no longer support the walls. The metallic plasma can then be trapped by the collapsing of the keyhole, nucleating spherical pores which are engulfed by the rapid solidification front before they can rise to the surface. The metallic vapors then condense and solidify leaving the porosity (**7, 40**). This type of defect is more likely to occur in welds that are processed at low beam power and/or short dwell time (low duty cycle). Increasing the specific energy input significantly increases the fusion time of the weld pool, allowing any nucleated pores to escape the molten material.

As traverse speed increases ($>$ 2 m/s), other defects tend to occur in laser welds, namely: surface holes, undercut and humping (**16**). Surface holes aligned at the center of the weld have been observed when using high temperature, high speeds, and power above 1.6 KW. It is caused by instability of the weld pool, and it is believed to be related to surface tension effects. Undercut, which shows as surface depressions along the weld at both sides of the fusion zone, and humping, which shows as a series of swellings (regular bulging and constriction) in the weld face, have been associated with surface tension effects and molten pool behavior.

CHAPTER 3

STATEMENT OF THE PROBLEM

Past research have shown that deposition welding reduces the high temperature strength of superalloys (**5**, **9**, **10**), In particular, a previous study on the effect of repair procedures, including brazing, TIG welding and electron beam welding (laser welding was not considered), found that the creep rupture strength of IN-738LC is reduced to values between 60 and 75% of the base alloy specification value (**10**).

Even though this specific study did not evaluate the origin of the reduction in the mechanical properties, the literature review on the subject indicated that this effect is related to:

- The formation of discontinuities in the HAZ due to the low general weldability of superalloys
- A disruption in the element and/or phase distribution in the fusion zone, that does not allow the alloy to attain of optimum strength upon heat treating

Laser deposition welding, using low strength filler metals (IN-625), has successfully been used to build up surface layers on regions of gas turbine components where mechanical stresses are low. These weld deposits can be produced with no detectable flaw indications by the non-destructive examinations (NDE) normally used on critical gas turbine parts, i.e., X ray and Fluorescent Liquid Penetrant. This indicates that it has been possible to adjust the welding parameters to produce sound welds within the effectiveness of these NDE techniques in locating flaws.

In order to determine the possibility of obtaining IN-738LC laser deposition welds with mechanical properties equivalent to those of the heat treated IN-738LC cast material, it is necessary to study two factors: the effect of the laser beam welding thermal cycle on the IN-738LC substrate and the response of the IN-738LC filler metal powder to laser fusion.

The effect of the laser beam welding thermal cycle on precipitation hardening alloys depends on the condition of the substrate, as well as on the welding parameters. The formation of cracks in the narrow HAZ produced by the laser beam welding process, including microcracks not detectable by the standard NDE techniques, is related to the ductility of the substrate (**21**). To increase the ductility and allow the material to relieve the residual stresses by creep or plastic deformation, it is possible to either dissolve the precipitates (solution anneal) or ripen the precipitates (age). Therefore, it is important to consider these pre-weld heat treating conditions.

The response of powder filler metal material to laser beam welding, on the other hand, is dependent upon the high surface temperatures and the high cooling rates produced by this high energy process. The characteristic temperatures of laser processing, typically greater than the boiling point of the alloy, may produce selective element vaporization that alters the chemical composition (**41, 42**). The high cooling rates originated by the low heat inputs may produce non equilibrium solidification that affects the precipitation of phases (**43, 44**). Therefore, both effects alter the element and phase distribution in the weld deposit. These metallurgical changes in the material can be studied by observing the element distribution and microstructure before and after the hardening heat treatments: 1) Solution Annealing followed by Aging or 2) Hot Isostatic Pressing (HIP) followed by Solution Annealing and followed by Aging.

CHAPTER 4

OBJECTIVES OF THE RESEARCH

The aim of this research was to determine the metallurgical conditions that would limit the mechanical strength of IN-738LC deposition welds applied by the laser beam welding process on IN-738LC substrate. The specific goals were the following:

- Determine the effect of substrate condition (as cast, solution and solution + age) on the formation of discontinuities in the heat affected zone, not detectable by the standard NDE techniques.
- Determine any significant chemical composition changes upon fusion of IN-738LC filler powder by the laser beam welding process.
- Determine the microstructural characteristics of the weld deposits after two post-weld hardening heat treatments (PWHT): (1) solution annealing + aging, and (2) Hip + solution annealing + aging.
- Evaluate any microstructural differences between the weld deposits and the cast structure, in the final heat treated condition.

CHAPTER 5

EXPERIMENTAL PROCEDURES

5.1- GENERAL APPROACH

The research was carried out in two main stages. The first stage was to adjust the welding parameters to obtain a sound weld deposit of IN-738LC powder over IN-738LC cast material. The starting parameters were those already being used for the deposition welding of IN-625 powder over IN-738LC cast material. This stage will be referred to as the Welding Procedure Qualification, and it involved the general steps shown in the flowchart of Figure 1.

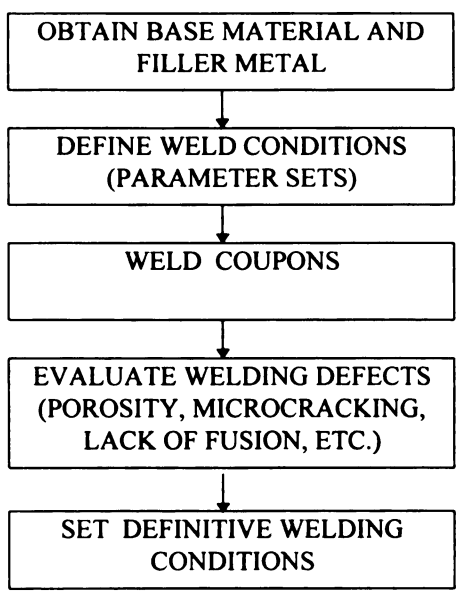

FIGURE 1- STAGE 1 FLOWCHART: Welding Procedure Qualification

The second stage was the actual study of the effects of substrate condition on the formation of discontinuities in the weld deposits, as well as the study of the effects of post-weld heat treatment on the microstructure of the weld deposits. The weld coupons used in the second stage were manufactured with the final parameters selected in stage 1. Figure 2 shows a flowchart of the general steps involved in this stage.

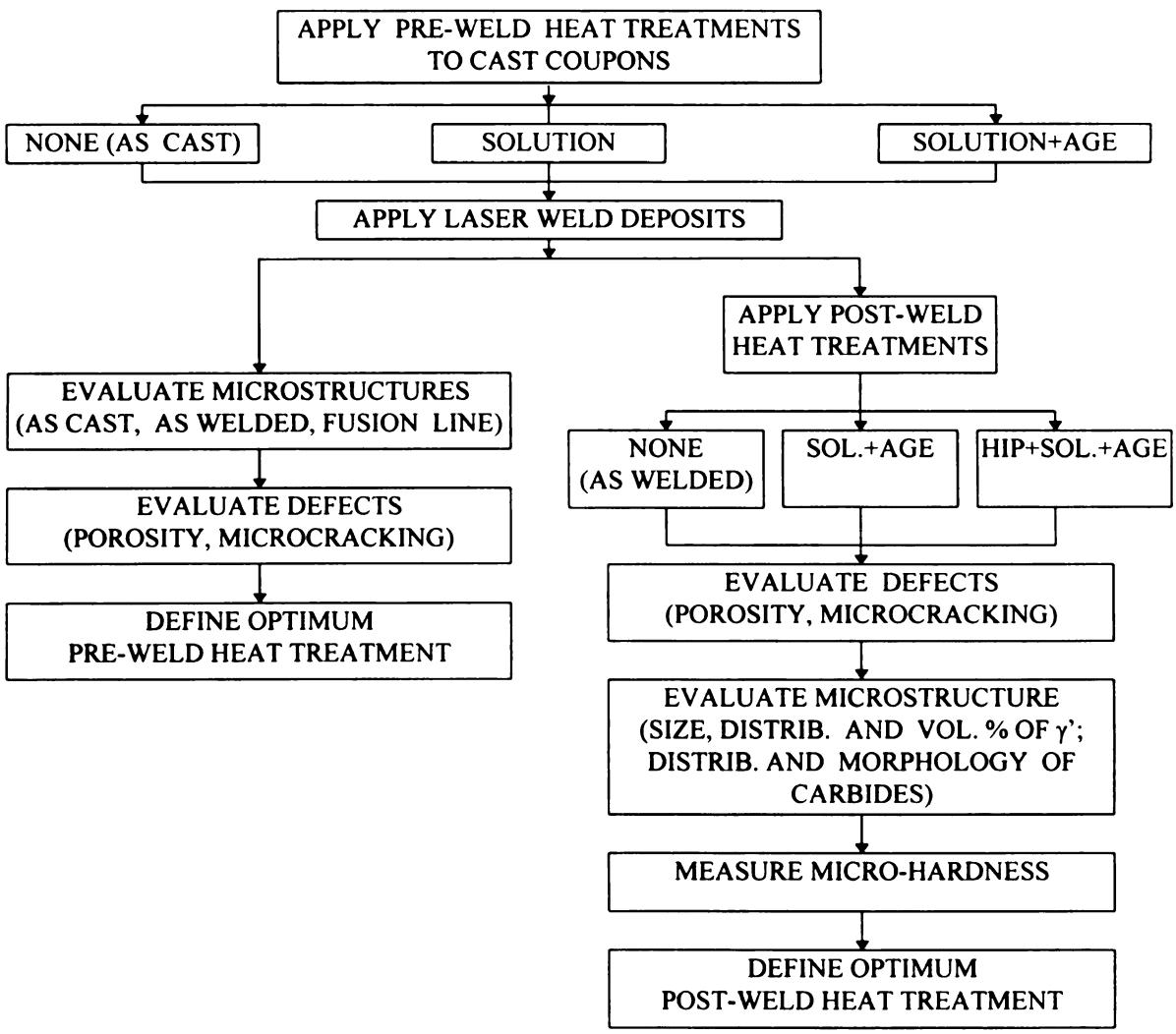

FIGURE 2- STAGE 2 FLOWCHART: Study of the Effects of Base Metal Condition and PWHT on IN-738LC Weld Deposit

5.2- MATERIALS

5.2.1- Substrate Material

The study of the response of superalloy IN-738LC base material to the laser weld overlay of IN-738LC powder was carried out on cast blocks of approximately 30 x 24 x 6 mm, which were prepared by vacuum induction melting of high purity materials. These test coupons were manufactured by Chromalloy Casting Tampa Corp., from a single heat which formed part of the regular production of vacuum investment cast turbine blades. Table 2 shows the results of the chemical analysis performed by the manufacturer along with the specification values. The samples were received as cast, without any previous thermo-mechanical or heat treatment.

TABLE 2- CHEMICAL COMPOSITION OF CAST ALLOY IN-738LC (REPORTED BY MANUFACTURER)

ELEMENT	SPEC. (wt %)	FOUNDRY (wt %)
C	0.09-0.13	0.11
Co	8.00-9.00	8.42
Cr	15.70-16.30	15.94
Mo	1.50-2.00	1.71
W	2.40-2.80	2.53
Ta	1.50-2.00	1.84
Nb	0.60-1.10	0.83
Al	3.20-3.70	3.44
Ti	3.20-3.70	3.28
B	0.007-0.012	0.008
Zr	0.03-0.08	0.05
Fe	0.50 max	0.46
Mn	0.20 max	0.12
Si	0.30 max	0.21
S	0.015 max	0.009
Ni	Balance	Balance

5.2.2- **Filler Powder**

The filler material used in this research was commercially available superalloy IN-738LC thermal spray powder, size -120/+325 mesh (45 to 125 μm), prepared by conventional argon atomization. This material was manufactured by Praxair Surface Technologies according to General Electric specifications ST1674. No general industrial standard is available for this particular product. Table 3 shows the results of the chemical analysis performed by the manufacturer.

TABLE 3- CHEMICAL COMPOSITION OF ALLOY IN-738LC POWDER

ELEMENT	SPEC. (wt %)	REPORTED (wt %)
C	0.09-0.13	0.11
Co	8.00-9.00	8.51
Cr	15.70-16.30	16.22
Mo	1.50-2.00	1.75
W	2.40-2.80	2.72
Ta	1.50-2.00	1.83
Nb	0.60-1.10	0.90
Al	3.20-3.70	3.40
Ti	3.20-3.70	3.60
B	0.007-0.012	0.011
Zr	0.03-0.08	0.055
Fe	0.50 max	0.10
Mn	0.20 max	0.05
Si	0.30 max	0.10
S	0.015 max	0.002
Ni	Balance	Balance

5.3- **LASER WELDING**

5.3.1- **Laser Welding System**

The deposition welds were carried out using a commercially available Huffman Model HP-113CL, CNC Laser Powder Welder, installed in the shops of Chromalloy

Heavy Industrial Turbine, Dallas, Texas. Chromalloy HIT is a repair shop specialized in the refurbishment of industrial gas turbine components for utility companies, as well as the oil and petrochemical industries, among others.

The welding system consisted of a 5 axis work table, vision camera, CNC control, laser unit and powder feeder.

The work table, with 3 linear and 2 rotational axes, was CNC controlled and assisted with a vision system to compensate for any contour configuration changes.

The heat source was a Rofin-Sinar RS-1700 SM, DC-exited, fast axial flow CO_2 industrial laser, with an output power range of 170 to 1900 watts. It can emit both continuous and pulse beam, at a wavelength of 10.6 μm, having a TEM_{10} (ring shape) spatial distribution. For the purpose of this experiment, the laser unit was operated in the continuous wave configuration.

The powder feeder unit was a self-contained station, METCO 9MP, which utilizes a weight-loss metering system to control feed rate. It works on the principle of fluidized beds, and can consistently deliver powder at rates as low as 0.07 g/s (0.5 lb/h).

The powder was carried through a hose to the nozzle by pressurized argon gas, where it was fed circumferentially around the laser beam. The nozzle regulated the appropriate amount of argon shielding gas to the alloy powder, and encased the focal point of the beam. This coaxial configuration brings the powder to the molten or quasi-molten state before it reaches the substrate. This increases the absorptivity of the beam energy in the fusion zone. Figure 3 shows the general configuration of the nozzle.

The laser welding system was designed to deposit beads in the range from 0.64 mm to 1.27 mm wide and 0.38 mm to 0. 76 mm in height, with a small amount of splatter.

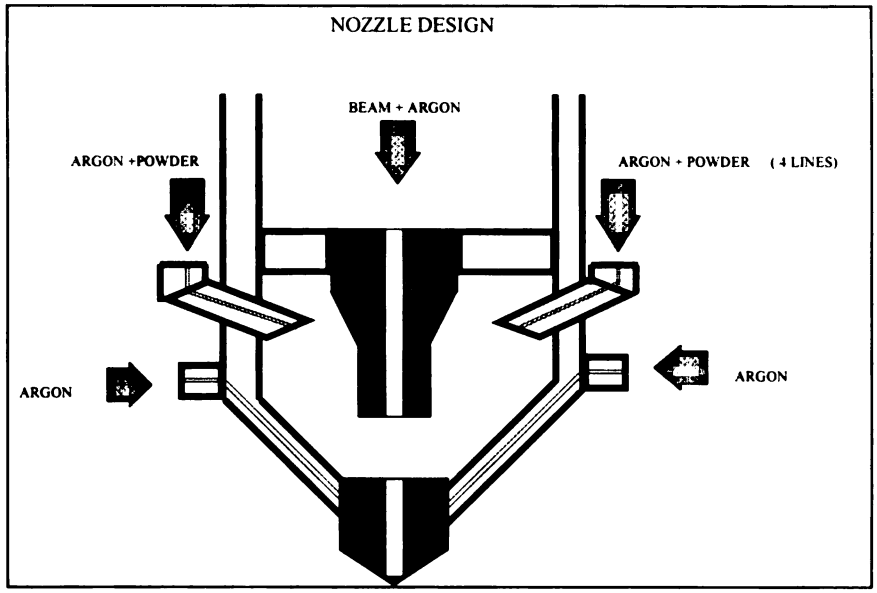

FIGURE 3- NOZZLE CONFIGURATION

5.3.2- **Process Parameters**

The welding parameters selected for this experiment were based on those already successfully used for the repair welding of IN-738LC turbine blades, using IN-625 filler powder. As mentioned before, IN-625 offers higher weldability, but lower mechanical strength.

Some welding parameters were fixed either by the welding system or based on previous experiences, while others were left as variables for the purpose of the welding procedure qualification.

Fixed Parameters

The type of nozzle used to deliver the powder fixed the focal position, the beam diameter and the nozzle to work-piece distance. The focal position and beam diameter

were set by the design of the system so as to optimize the energy input during the welding process. Since the exact position of the focal point and the diameter of the beam were not given in the equipment specifications, a test was performed to determine their values. After removing the nozzle, an aluminum sheet coated with a thin film of acrylic paint was subjected to short laser beam pulses of constant power (60 watts). By varying the position of the aluminum sheet in the "Z" axis (positive sense towards the work piece), and measuring the diameter of the burned area, the focal position was found to be at approximately 5 mm above the nozzle tip, as shown in Figure 4.

Similarly, the nozzle to work-piece distance was fixed by the design of the system to 3.81 mm (0.150 in), which allowed for the powder particles to reach the base material in the molten or quasi-molten state, and minimized the clogging of the nozzle by any powder particles bouncing back from the weld pool. The diameter of the beam at this point was found to be approximately 1.20 mm, as shown by Figure 4.

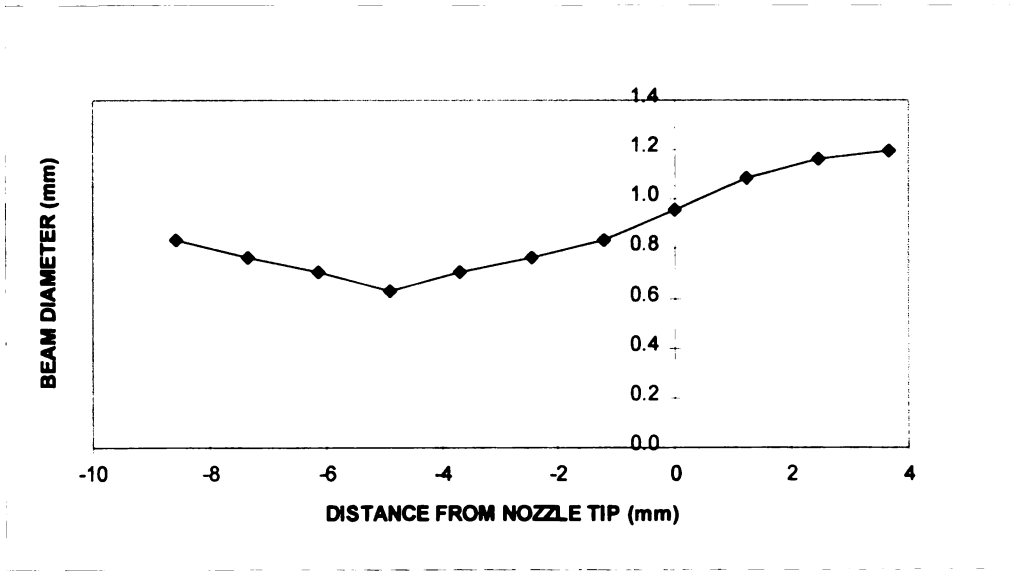

FIGURE 4- DETERMINATION OF FOCAL POINT

The shielding gas and its flow was also fixed to argon at 0.28 m^3/h (10 cfh), which ensure an adequate protection from oxidation as based on previous superalloys welding experiences.

Variables

The only variables considered were power, traverse speed and feed rate, which for deposition welds of alloy IN-625 are set at the values presented in Table 4. In order to adjust the values for the deposition welding of alloy IN-738LC, three conditions at higher energy input and 4 conditions at lower energy input were selected for a welding qualification process. Higher energy inputs would allow higher deposition rates with its corresponding economic incentive, while lower energy inputs would minimize the possibility of cracking.

TABLE 4- INITIAL WELDING PARAMETERS

Variable	Power	1230 W
	Traverse Speed	8.9 mm/s (21 in/min)
	Feed Rate	0.08 g/s (0.6 lb/h)
Fixed	Beam Diameter	1.20 mm (0.049 in)
	Focal Position	-5.00 mm (-0.200 in) from nozzle tip
	Shielding Gas	Argon / 0.28 m^3/h (10 cfh)
	Nozzle-Work piece Distance	3.81mm (0.150in)

The feed rate was maintained at the lower end of the operational range of the feeder system (0.066 and 0.083 g/s, corresponding to 4 and 5 g/min), while traverse speed was adjusted at the highest possible value that would yield a smooth stable bead (8.3 and 9.3 mm/s, corresponding to 19.5 and 21 in/min).

The variables selected for the welding qualification process, along with the power density and energy input for each condition are presented in Table 5. Condition 4 corresponds to the base welding parameters (IN-625 welding procedure).

TABLE 5- VARIABLES CONSIDERED IN WELDING PROCEDURE QUALIFICATION

CONDITION	POWER (W)	TRAVERSE SPEED (mm/s)	FEED RATE (g/s)	POWER DENSITY (W/mm^2)	ENERGY INPUT (J/mm)
1	1305	8.30	0.083	1150	157.2
2	1260	8.30	0.083	1115	151.8
3	1240	8.30	0.066	1097	149.4
4	1230	8.30	0.083	1088	148.2
5	1230	9.30	0.083	1088	132.3
6	1190	9.30	0.066	1053	128.0
7	1100	9.30	0.066	973	118.3
8	1080	9.30	0.066	955	116.1

5.3.3- **Welding Procedure Qualification**

Multiple pass deposition welds, measuring 30 mm in length, 10.5 mm in width (corresponding to approximately 10 adjacent beads) and 5 mm in height (corresponding to approximately 6 welding passes), were applied over the substrate material using each one of the 8 conditions referred in the previous section. Figure 5 shows a general view of one of the deposition welds.

The quality of the deposition welds was determined by visual inspection of the external surfaces using a binocular microscope (7.5 to 64X), and by quantifying the amount of internal discontinuities as measured by an image analyzer (the equipment specifications are presented in Section 5.5). The quantification of indications for each

set of variables was done on unetched metallographic samples prepared on the surface of three sections cut perpendicular to the weld axis.

The discontinuities were classified into spherical and linear, since it was possible for the image analyzer to accurately separate welding porosity, which tends to be spherical in nature, from weld cracks which tend to be closed and unbranched, as confirmed by metallographic observations. Other irregularly shaped discontinuities, such as lack of fusion, were manually separated from the image plane. Therefore, the automatic quantification was exclusively performed on spherical and linear indications.

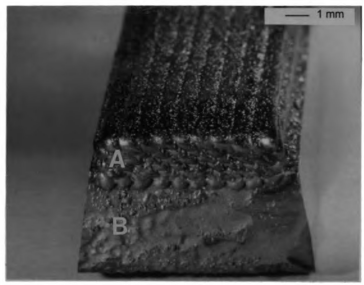

FIGURE 5- GENERAL VIEW OF DEPOSITION WELD COUPON
(A- Weld Deposit, B- Base Material)

The analysis was done at the minimum magnification allowed by the binocular microscope (7.5X), in order to include the largest possible surface area. The minimum detectable spherical indication was 0.07 mm in diameter and the minimum detectable linear indication was 0.21 mm in length, which corresponds to values below the maximum sensitivity of standard non-destructive testing techniques (industrial radiography and fluorescent liquid penetrant). Linear indications were defined as those having an aspect ratio greater than 5:3.

5.4- THERMO-MECHANICAL AND HEAT TREATMENTS

The hot isostatic pressing of the deposition weld coupons was done on an Eagle 6 HIP system, manufactured by International Pressure Services. This system includes a water cooled vessel rated for a maximum of 207 MPa working pressure, connected to an electro-hydraulic gas compressor. The vessel contains a molybdenum element furnace with a maximum attainable temperature of 1823 K (temperature stability -0/+15 K at steady state), and a 114 mm diameter by 140 mm long hot zone. The temperature was monitored by two thermocouples located at the top and bottom of the furnace.

The system also included a mechanical vacuum pump which allowed vacuum/argon pressurization cycles to minimize the high temperature oxidation of the samples. The temperature and pressure were controlled by a microprocessor-based programmable controller, and the actual cycle was registered by a chart recorder. The high cooling rates required by the thermal cycles were obtained by rapidly depressurizing the vessel.

The solution and aging treatments were carried out in a bench-top Lindberg 58114 wire element furnace with a microprocessor-based controller. It had a 1473 K temperature rating and a stability of -5/+5 K at steady state.

FIGURE 6- THERMO-MECHANICAL AND HEAT TREATMENT CYCLES

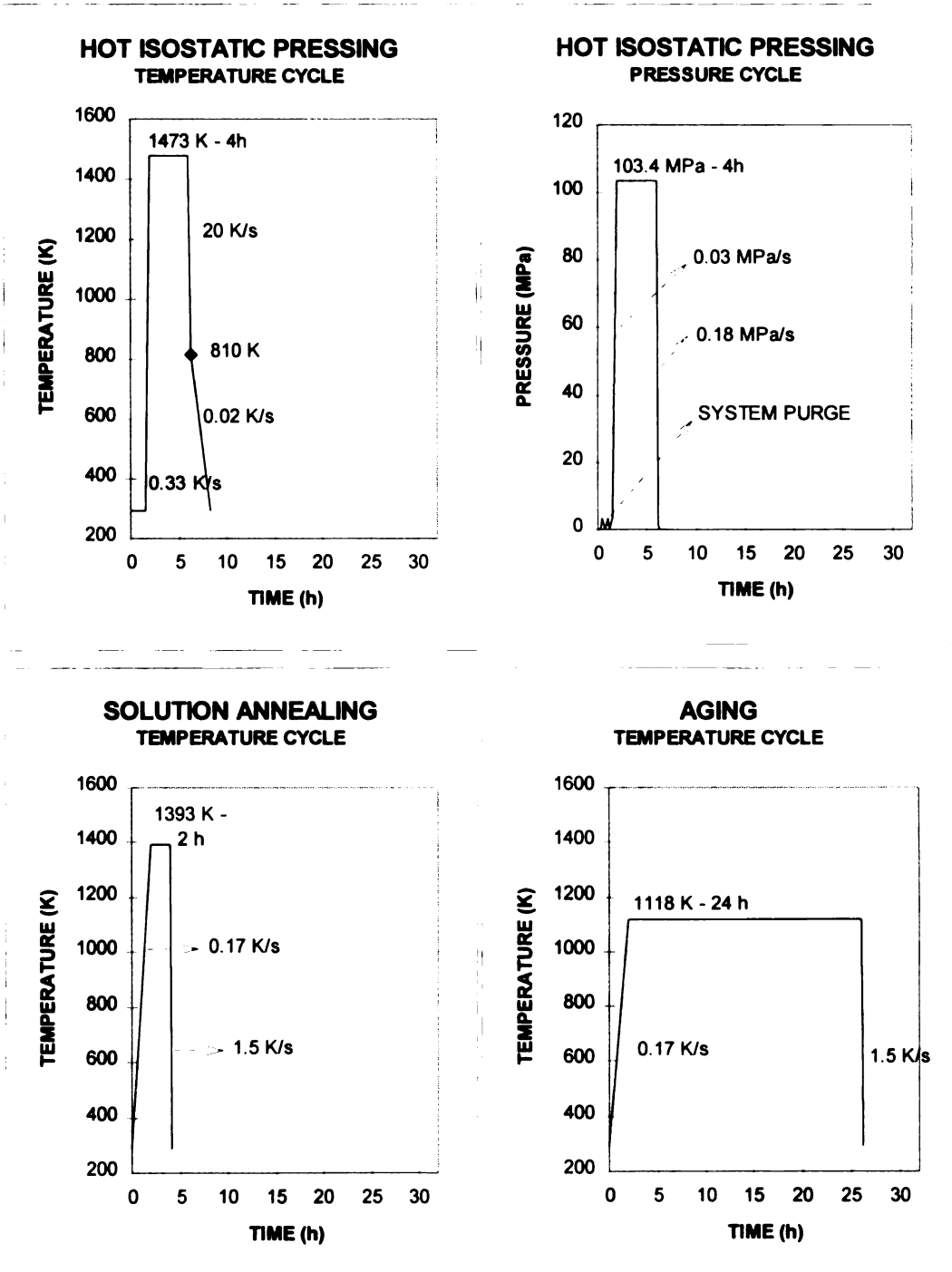

The thermo-mechanical and heat treatment cycles applied to the weld coupons were those stated in the specification for the manufacturing of nickel-base IN-738LC investment casting alloys, as presented in Section 2.1.4. Figure 6 shows graphical representation of the cycles.

For the HIP cycle, the heating rate was set at 0.33 K/s. The cooling rate from the holding temperature down to 810 K was set at 20 K/s, in order to minimize the uncontrolled precipitation and growth of γ'. This cooling rate was achieved by venting the argon gas contained in the pressure vessel from 103 MPa (15000 psi) to 1.4 MPa (200 psi) in 300 seconds. The cooling rate from 810 K to room temperature was that attained inside the furnace (approximately 1.87 $x10^{-2}$ K/s).

For the solution and aging cycles, the heating rate was set at 0.17 K/s, while air cooling was used to cool the specimen to room temperature (approximately 1.5 K/s).

5. 5- MICROSTRUCTURAL CHARACTERIZATION AND CHEMICAL ANALYSIS

The structures of the base material and weld deposits were studied by standard metallographic techniques through light microscopy (LM) and scanning electron microscopy (SEM). Additionally, the size of microporosity, microcracking and precipitates, as well as the area fraction of phases, were quantified by means of a digital image analyzer. Grain sizes were determined by the linear intersection method as established by the standard ASTM E112. Specifically, the equipment used for microstructural observation was the following:

- Olympus PME-3 optical microscope
- JEOL JSM-6400V field emission scanning electron microscope
- LECO 2001 image analysis system

In order to study each particular feature of the microstructure (dendritic structure, grain size, microsegregation, γ' and carbides), several chemical and electrolytic reagents presented in the literature were evaluated **(25, 26, 28, 29, 45, 46, 47).** Table 6 shows the procedure used for specimen preparation, including the reagents that showed the best feature definition, as well as the parameters involved. The next chapters will refer to these reagents by the numbers assigned in this Table 6.

TABLE 6- SPECIMEN PREPARATION PROCEDURES

TECHNIQUE	PROCEDURE	REAGENT	PARAMETER	FEATURE
Light Microscopy	Mechanical Polish			
	Chemical Etch	#1 10 g $CuSO_4$ 50 ml HCl 50ml H_2O	40 s	Grain Boundaries
	Chemical Etch	#2 1.5 g $CuCl_2$ 33 ml ethanol 33 ml HCl 33 ml H_2O	20 s	Segregation
Scanning Electron Microscopy	Electropolish	#3 20 ml $HClO_4$ 180ml Methanol	0.01 A/mm^2 20 s	
	Electro Etch	#4 170 ml H_3PO_4 10 ml H_2SO_4 16 g CrO_3	0.01 A/mm^2 2 s	General microstruct.
	Chemical Etch	#5 2 g $CuCl_2$ 50 ml HCl 25 ml HNO_3 200 ml H_2O	15 s	γ' measurement
	Chemical Etch	#6 10 g $CuSO_4$ 50 ml HCl 50 ml H_2O	10 s	Carbide distribution

Qualitative and semi-quantitative chemical analysis of the phases were carried out by Energy Dispersive X-Ray spectroscopy, on a Tractor TN-5500 EDX System, which was attached to the SEM.

Finally, quantitative chemical analyses by the Inductively Coupled Plasma (ICP) techniques were carried out on the cast material, powder filler metal and weld deposit, to verify compliance to the specification, and to determine any element loss during the welding process. These analyses were performed and certified by an external laboratory. The results have a precision of +/- 0.05 %.

5. 6- **HARDNESS MEASUREMENTS**

The microhardness determinations were carried out in a LECO M-400-G1 micro hardness tester, with a 500 g mass indenter. The indention time was set at 15 seconds.

Hardness scans were taken across the fusion line in increments of 0.1 mm, covering a distance of 1.45 mm on each side. Each reported value corresponds to the mean of three individual determinations.

CHAPTER 6
RESULTS AND DISCUSSION

6.1- MATERIALS VERIFICATION ANALYSIS

The results of the quantitative chemical analyses performed on samples of the cast blocks and filler powder are presented in Table 7. The elements analyzed correspond to the main alloy components, which include the base element (Ni), the two main solid solution strengtheners (Cr and W), the γ' formers (Al and Ti), and the promoter of γ' precipitation (Co).

TABLE 7- RESULTS OF VERIFICATION CHEMICAL ANALYSIS

ELEMENT	SPECIFICATION (wt %)	POWDER (+/- 0.05 wt %)	CAST BLOCK (+/- 0.05 wt %)
Ni	58.18 - 63.80	61.61	61.71
Cr	15.70 - 16.30	15.95	16.02
W	2.40 - 2.80	2.58	2.60
Al	3.20 - 3.70	3.64	3.68
Ti	3.20 - 3.70	3.47	3.50
Co	8.00 - 9.00	8.52	8.54

As can be observed in Table 7, both the chemistry of the cast block material and filler powder material are within the limits set by the specification.

Additionally, since the characteristics of the powder (morphology and size distribution) have an effect on the performance of the nozzle (coaxial feed type), SEM observations were made on a sample of powder spread over an area of 78.5 mm^2 (10 mm diameter SEM stub).

Figure 7 shows a view of the powder, which is composed mainly of spherical particles with a small amount of modular particles (rounded irregular shaped). No angular particles or foreign material, were detected.

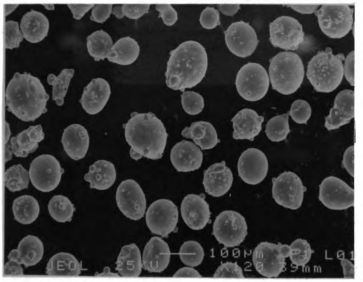

FIGURE 7 - GENERAL VIEW OF THE POWDER PARTICLES

By using the image analyzer, a population of 201 particles was measured, giving the uniform size distribution presented in Table 8. The obtained values were within the limits set by the product specification.

TABLE 8- PARTICLE SIZE VERIFICATION ANALYSIS

SIZE RANGE (mesh)	SPEC. VALUE (wt%)	MEASURED VALUE (wt %)
+120	0.0-0.5	0.0
-120/+325	84.5 min	99.8
-325	0.0-15.0	0.02

6.2- WELDING PROCEDURE QUALIFICATION RESULTS

6.2.1- General Observations

All the deposition weld coupons, corresponding to the eight conditions referred in Table 5, showed a smooth external finish with little splatter. No externally open cracks were visually detected. Figure 8 shows a view of the external surface appearance of one of the coupons.

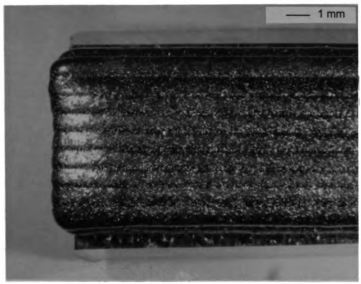

FIGURE 8- TOP VIEW OF DEPOSITION WELD COUPON

As it was indicated in section 5.3.3, the internal discontinuities detected in perpendicular sections of the weld coupons were quantified. Figure 9 shows a view of one of the sections which was macro-etched for the purpose of delineating the weld beads.

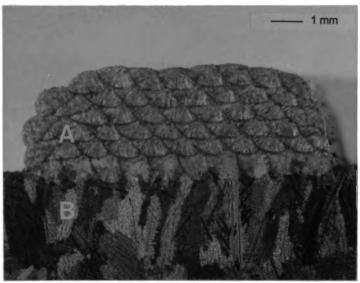

FIGURE 9- TRANSVERSE SECTION OF DEPOSITION WELD COUPON
(Macro-etched, Reagent #1 / A-Weld Deposit, B-Base Material)

The discontinuities detected were mainly porosity and cracking. While porosity was uniformly distributed throughout the weld deposit, cracks tended to be concentrated at the center of beads and in the base material-weld deposit fusion line. Figures 10 and 11 display the types of indications detected.

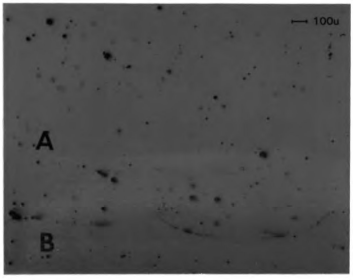

FIGURE 10- GENERAL VIEW OF POROSITY IN THE WELD DEPOSIT
(Unetched / A-Weld Deposits, B-Base Material)

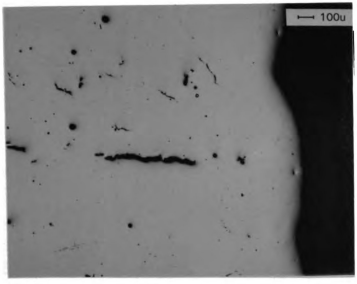

FIGURE 11- GENERAL VIEW OF CRACKING IN THE WELD DEPOSIT
(Unetched)

Welding condition 8 (as noted in Table 9), which was set at the lowest power density (955 W/mm^2), additionally showed lack of fusion between the weld deposit and the base material, as well as between weld passes (Figure 12). This indicates that the energy input obtained with this set of parameters was not capable of producing an adequate melting of the base metal and the powder particles. This also indicates that condition 7, which was set at slightly higher power density (973 W/mm^2), and which did not show this type of defect, was close to the minimum energy required for producing a well fused deposit.

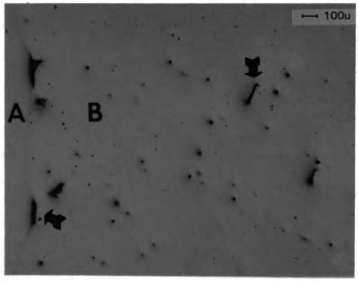

FIGURE 12- SECTION OF WELD COUPON MANUFACTURED UNDER CONDITION 8
(Unetched / A- Base Material, B- Weld Deposit, arrows mark lack of fusion)

ılength

set of

and sp

show t

6.2.2- **Quantification of Indications**

Table 9 shows the values for the number of counts and main characteristic (length or area) for each type of indication, as well as the total area analyzed for each set of variables. As it can be observed from the standard deviation values, both linear and spherical indications showed a wide range of sizes. Table 10 and Figures 13 to 15 show the above results expressed in area density.

TABLE 9- QUANTIFICATION OF INDICATIONS IN WELDING PROCEDURE QUALIFICATION

LINEAR INDICATIONS

CONDITION	FEATURE COUNT	TOTAL LENGTH (mm)	AVERAGE LENGTH (mm)	STANDARD DEVIATION	AREA ANALYZED (mm^2)
1	8	3.589	0.449	0.350	94.04
2	11	4.220	0.384	0.386	141.06
3	17	13.496	0.794	0.659	74.96
4	12	5.193	0.433	0.411	140.19
5	45	14.449	0.321	0.083	93.04
6	55	24.903	0.453	0.217	139.57
7	4	1.059	0.265	0.050	139.51
8	45	18.822	0.418	0.166	139.58

SPHERICAL INDICATIONS

CONDITION	FEATURE COUNT	TOTAL AREA (mm^2)	AVERAGE AREA (mm)	STANDARD DEVIATION	AREA ANALYZED (mm^2)
1	19	1.458	0.077	0.0022	94.04
2	71	0.594	0.008	0.0035	141.06
3	16	0.121	0.008	0.0029	74.96
4	16	0.127	0.008	0.0017	140.19
5	33	0.384	0.012	0.0044	93.04
6	32	0.281	0.009	0.0039	139.57
7	23	0.181	0.008	0.0042	139.51
8	132	1.081	0.008	0.0033	139.58

TABLE 10- INDICATIONS DENSITY IN WELDING PROCEDURE QUALIFICATION

CONDITION	LINEAR DEFECTS DENSITY		SPHERICAL DEFECTS DENSITY	
	(Counts/mm^2)	(mm/mm^2)	(Counts/mm^2)	(mm^2/mm^2)
1	0.085	0.038	0.202	0.016
2	0.078	0.030	0.503	0.004
3	0.227	0.180	0.213	0.002
4	0.086	0.037	0.114	0.001
5	0.484	0.155	0.355	0.004
6	0.394	0.178	0.229	0.002
7	0.029	0.008	0.165	0.001
8	0.322	0.135	0.946	0.008

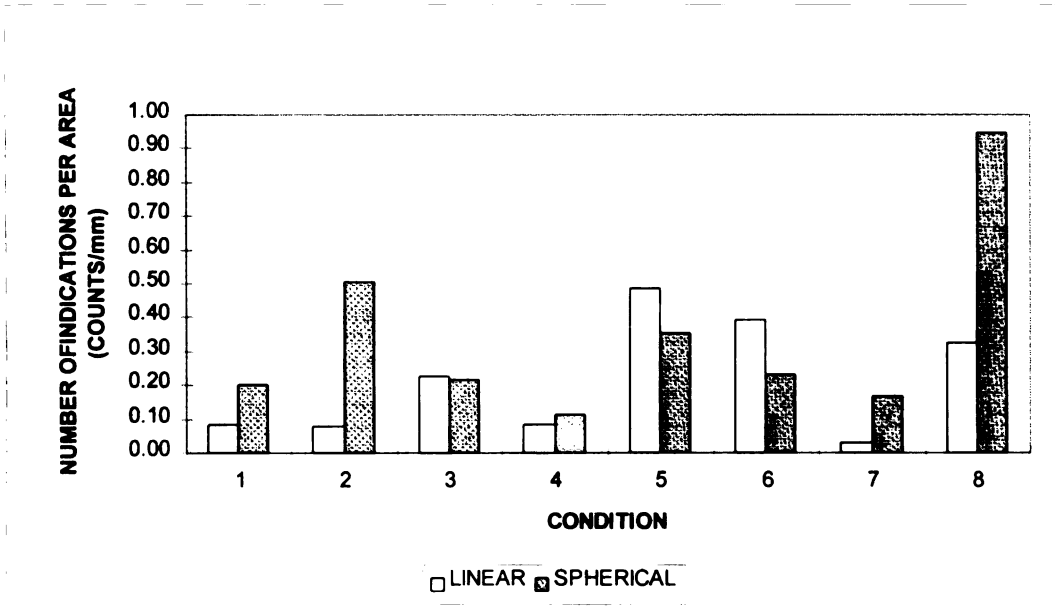

FIGURE 13- LINEAR AND SPHERICAL INDICATIONS DENSITY

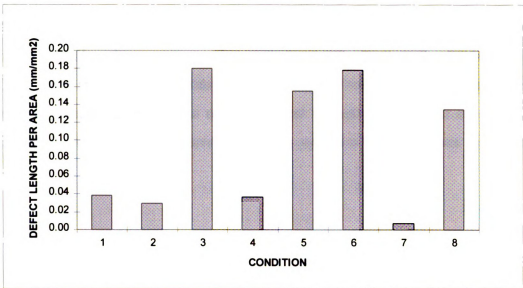

FIGURE 14- LINEAR INDICATIONS LENGTH DENSITY

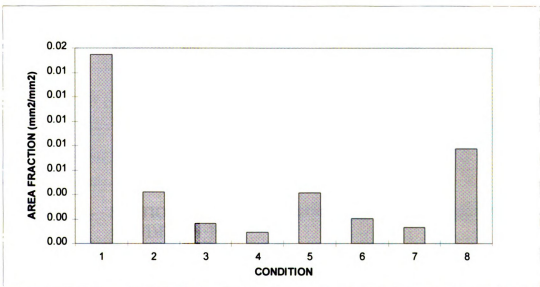

FIGURE 15- SPHERICAL INDICATIONS AREA FRACTION

As it can be observed in the bar charts, conditions 4 and 7 show the least amount of indications. Condition 7 shows 62% fewer linear indications, as well as 78% shorter crack length per unit area than condition 4. On the other hand, condition 4 shows 31% fewer spherical indications than condition 7. Considering that linear defects are intrinsically more detrimental to the mechanical strength of the weld deposit than spherical defects, the parameters corresponding to condition 7 were chosen for further study.

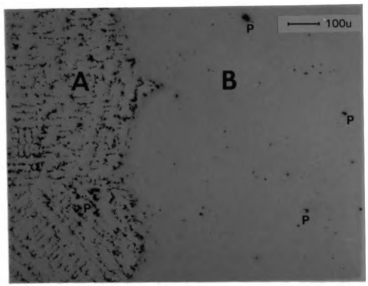

FIGURE 16- SECTION OF WELD COUPON MANUFACTURED UNDER CONDITION 7
(Reagent # 1 / A- Base Material, B- Weld Deposit, P- Porosity)

Table 11 shows the selected parameters, which were fixed for the analysis of the effect of base metal condition and post-weld heat treatment on the

microstructure of the deposition welds. Figure 16 shows a view of a section perpendicular to a weld coupon manufactured according to the parameters of condition 7. It displays less porosity and crack density than figures 10 and 11. It also shows interdendritic porosity in the base material, which is comparable to the level of porosity in the weld deposit.

TABLE 11- SELECTED WELDING PARAMETERS

Variable	Power	1100 W
	Traverse Speed	9.3 mm/s (22 in/min)
	Feed Rate	0.07 g/s (0.5 lb/h)
Fixed	Beam Diameter	1.20 mm (0.049 in)
	Focal Position	-5.00 mm (-0.200 in) from nozzle tip
	Shielding Gas	Argon / 0.28 m^3/h (10 cfh)
	Nozzle-Work piece Distance	3.81mm (0.150in)

6.2.3- **Weld Deposit Chemical Verification Analysis**

In order to determine any significant chemical changes associated with vaporization of the alloy elements, quantitative chemical analyses (ICP) were performed on two deposition weld samples. The results, together with the specification required and the analysis of the powder, are presented in Table 12.

As it can be observed in Table 12, the results are within the limits established by the specification of the alloy. Additionally, the IN-738LC weld deposit chemistry falls within the measurement error of the IN-738LC powder filler chemistry (+/- 0.05%). This indicates that no significant composition variation occurred during the

welding process, as far as the sensetivity limits of the Inductively Coupled Plasma technique allow to measure.

TABLE 12- WELD DEPOSIT CHEMICAL ANALYSIS RESULTS

ELEMENT	SPECIFICATION (wt %)	POWDER (wt %)	WELD DEPOSIT (wt %)		
			Sample 1	Sample 2	Mean
Ni	58.18 - 63.80	61.61	61.58	61.55	61.56
Cr	15.70 - 16.30	15.95	15.82	15.96	15.89
W	2.40 - 2.80	2.58	2.58	2.58	2.58
Al	3.20 - 3.70	3.64	3.63	3.65	3.64
Ti	3.20 - 3.70	3.47	3.45	3.47	3.46
Co	8.00 - 9.00	8.52	8.48	8.54	8.51

6.3- BASE MATERIAL CONDITION EFFECTS ON LASER DEPOSITION WELDS

6.3.1- Microstructural Evaluation of Base Material

As Cast Condition

The material showed the basic features presented in Section 2.1.4, that is, a microstructure characterized by a large variation in precipitate sizes and morphology. The structure consisted of elongated grains of γ phase containing well defined branched dendrites (equiaxed dendritic morphology). The mean primary arm spacing, as measured on micrographs, was 93 μm. The grain size, as measured by the intercept technique, was found to be ASTM No. 2.4.

The grain boundaries were defined by a high concentration of carbides at interdendritic spaces. Microporosity was also observed in the interdendritic regions, both at intergranular and intragranular sites. Figure 17 shows a general view of the microstructure at low magnification.

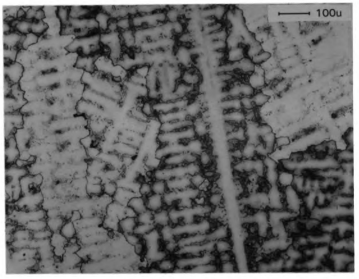

FIGURE 17- GENERAL MICROSTRUCTURE IN AS CAST MATERIAL (Reagent # 1)

It was also observed, by means of the appropriate etching reagent, that the structure was heavily cored, indicative of a segregated structure (Figure 18). Segregation is the result of variations in the solubility of the alloy elements during solidification, which causes accumulation of solute in the interdendritic spaces or dendritic arm regions. A previous study showed that the distribution coefficients, k, for alloy IN-738LC, defined as the ratio of solute concentration in the solid and in the liquid for each alloy element, are the ones presented in Table 13 (**48**).

TABLE 13- DISTRIBUTION COEFFICIENTS OF ALLOY IN-738LC

ELEMENT	W	Al	Co	Ni	Cr	Mo	Ta	Ti	Nb	Zr
k	1.40	1.20	1.10	1.05	1.05	0.85	0.70	0.60	0.40	0.06

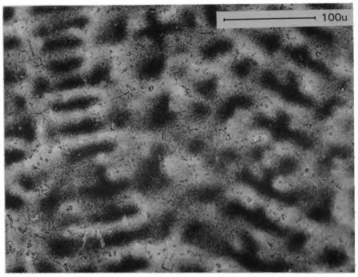

FIGURE 18- CORE SEGREGATION IN AS CAST MATERIAL
(Reagent # 2)

According to these values, the expected migration of the elements during solidification is the following:

- W, Al and Co segregate to dendrite core regions ($k > 1$)
- Ni and Cr adopt a homogeneous distribution ($k \approx 1$)
- Mo, Ta, Ti, Nb and Zr segregate to the interdendritic regions ($k < 1$)

This complex element behavior results in microinhomogeneities with the scale and periodicity of the dendrite arm spacing, which in turn produces the characteristic microstructure revealed at high magnification, as shown in Figure 19. Figure 20 shows EDX x-ray maps of the main alloy elements. The high concentration of Ta, Ti, Nb and Zr detected in this region is in agreement with the segregation behavior explained above.

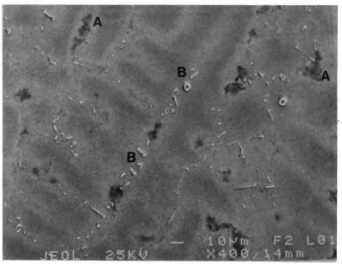

FIGURE 19- PRECIPITATE PHASES IN AS CAST IN-738LC
(Reagent # 6 / A-Eutectic γ', B-Carbides at Interdendritic Spaces, cubic γ' is not resolved)

Two types of γ' are present in this structure: eutectic γ', composed of massive particles of γ' separated by thin lamellae of γ, which provides little strength to the material (**49**), and finer cuboidal γ', which is the main strengthening precipitate. Figure 21 shows both types of γ' after selectively etching the matrix. Figure 22 shows the skeleton of γ lamellae in eutectic γ' after selectively etching the γ' phase.

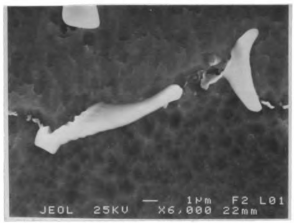

Ta (M_α - 1.71 KeV)

FIGURE 20- EDX DOT MAPPING OF PRECIPITATES AT INTERDENDRITIC REGION (Reagent # 6)

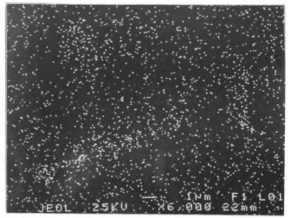

Nb (L_α - 2.17 KeV)
Zr (L_α - 2.04 KeV)

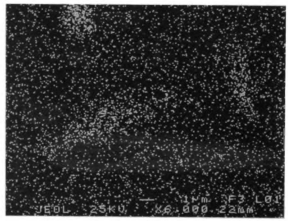

Ti (K_α - 4.51 KeV)

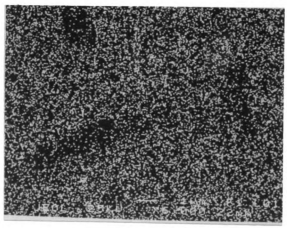

Cr (K_α - 5.41 KeV)

FIGURE 20 (cont'd).

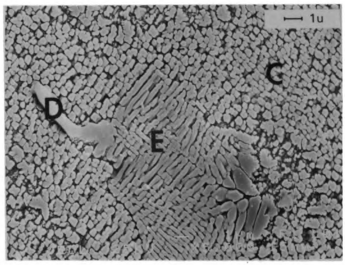

FIGURE 21- γ' PHASE IN AS CAST IN-738LC
(Reagent # 4 / C- Cuboidal γ', E- Eutectic γ', D- Carbide)

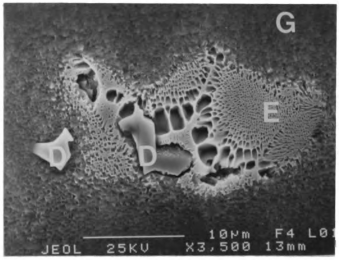

FIGURE 22- γ PHASE IN AS CAST IN-738LC
(Reagent # 5, / G- γ Matrix, E- Eutectic γ Skeleton, D- Carbides)

The eutectic γ' heterogeneously precipitates from the supersaturated liquid phase during dendritic solidification. It nucleates on small γ-γ' nuclei that constitute the last fraction of melt to freeze, consequently, it is mainly present at dendrite tips and grain boundaries. On the other hand, cuboidal γ' homogeneously precipitates in the solid material that is supersaturated with the γ' forming elements (Al, Ti and Nb) and it is finely dispersed throughout the matrix (**45**).

The microstructure also showed two types of carbides with different morphology and composition, as can be observed in Figure 23. Large rod-shape or "chinese script" carbides were found in the interdendritic regions, both at grain boundaries and in the inner grains, while smaller spheroidal carbides were found to form chains of discrete particles along the grain boundaries.

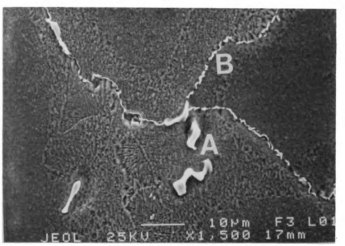

FIGURE 23- GENERAL VIEW OF CARBIDES
(Reagent # 6 / A-Script Carbides, B-Spheroidal Carbides)

Figure 24 shows the results of Energy Dispersive X-Ray analyses performed on the matrix and on both types of carbides. The script-shape Ti/Ta-rich particles correspond to MC type carbides, while the spheroidal-shape Cr-rich particles correspond to $M_{23}C_6$ type carbides. Both types of carbides have been previously characterized and they are a distinctive feature of alloy IN-738LC (**46, 49, 50, 51**).

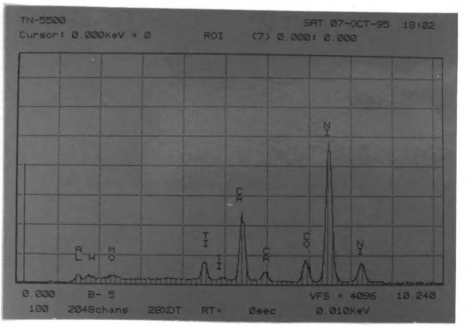

A

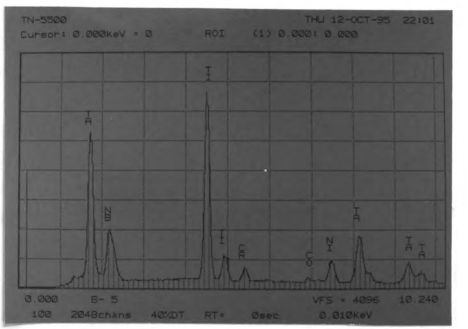

B

FIGURE 24- EDX ANALYSES RESULTS
(A- Matrix, B- Script Carbides, C- Spheroidal Carbides)

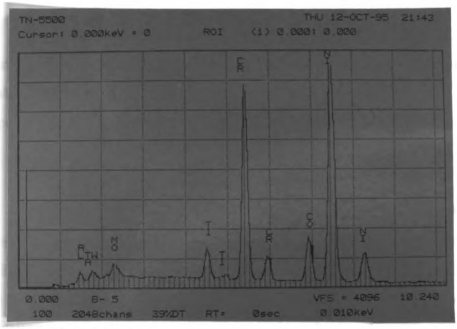

C

FIGURE 24 (cont'd)

Similar to the formation of eutectic γ', the formation of MC carbides is related to interdendritic segregation of refractory elements. The addition of 1.75% Ta to IN-738LC to improve the stability of γ', promotes the precipitation of the high Ta content MC carbide, although Ti is also present (**50**). This type of carbide is very stable at high temperatures. It has been observed that it remains present in the alloy melt above the liquidus temperature up to 1868 K (**20**). However, it transforms to $M_{23}C_6$ during long time exposure (> 3000 h) at temperatures below 1144 K.

The $M_{23}C_6$ spheroidal type carbide, on the other hand, differs from MC type carbide in that it forms by solid state precipitation at grain boundaries on cooling, after solidification is complete. The discrete morphology has been found to optimize creep-rupture life by preventing grain boundary sliding, while providing sufficient ductility in the surrounding grain for stress relaxation to occur without premature failure (**43**). When no grain boundary precipitates are present, grain boundary movement is unrestricted, leading to subsequent cracking at grain boundaries triple points.

As can be observed in the previous micrographs (Figures 19 and 23), both types of carbides are present in small relative amounts. The reason for this is that the available carbon in the alloy (0.13 wt %) can only yield a maximum of 1.2 vol % of precipitated carbide phase **(52).**

Heat Treated Condition

The microstructures of both solution annealed and FHT alloy show the same general features as the as cast alloy, except that there is a refinement in the size and morphology of the γ' precipitate in the heat treated condition. This refinement is the result of a homogenization effect produced by the heat treatments. Figure 25 shows a comparison between the microstructures of the different pre-weld conditions around script carbides (interdendritic regions). The as-cast material shows irregularly shaped γ' with a wide range of sizes, the solutionized material shows a very fine dispersion of γ', and the solutionized + aged material shows a dispersion of larger γ' in the interdendritic regions and smaller particles in the dendritic core region.

A.- Solutionized Condition

The phase transformations that yield the refinement of the γ' can be described as follows:

1. Due to the segregation process that takes place during solidification, in the dendrite core regions the concentration of Al and Ti is below their solubility product at the solution treatment temperature (1393 K), thus allowing the solutionizing of the γ' in the γ matrix. On the other hand, in the interdendritic regions the concentration of Al and Ti is higher, and the treatment temperature required for solutionizing the γ' is above the actual solutionizing temperature. Therefore, part of the primary γ' may only be partially dissolved. Particularly, the eutectic γ' is normally unaffected by the solutionizing treatment **(53)**

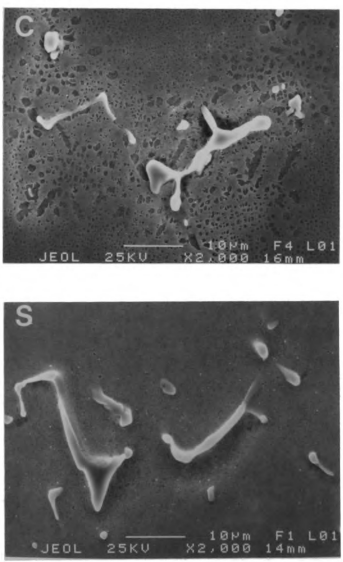

FIGURE 25- CHARACTERISTIC MICROSTRUCTURES OF THE PRE-WELD CONDITIONS
(Reagent #5, C-As Cast, S-Solution, A-Solution + Age)

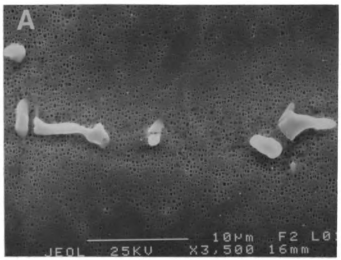

FIGURE 25 (cont'd.)

2. During the air cooling stage, due to the fast kinetics of the γ' precipitation reaction, a fine secondary γ' precipitate forms uniformly throughout the matrix. In the interdendritic regions, it forms around the undissolved primary γ', however, it is restricted in size, due to the low concentration of Al and Ti in the immediate vicinity of these particles.

The result is then a uniform distribution of small globular secondary γ' particles in the dendritic core regions, and a bimodal distribution of larger cuboidal primary γ' particles surrounded by smaller secondary γ' particles in the interdendritic regions. Since there is only a short time for the γ' to grow during the cooling stage, below the solvus temperature, both the primary and secondary particle sizes are refined with respect to the size of γ' in the as cast microstructure, as shown in Figure 25S.

As it was previously indicated, MC carbides are very stable at high temperature and remain undissolved at the solutionizing temperature. Consequently, there is no detectable change in their size or morphology after the solution annealing. On the other hand, the $M_{23}C_6$ carbide solvus temperature is 1273 K (**51**), which is below the solution annealing temperature; therefore, this carbide goes into solution. However, during cooling it reprecipitates at the grain boundaries as discrete spheroidal particles. The final result is then a carbide distribution equivalent to that of the cast structure.

B.- Solution + Age

The effect of the aging treatment is the coarsening of the γ' resulting from the solution anneal cycle, as well as the precipitation of new fine γ' in the dendritic core regions. This secondary γ' forms from the Al and Ti that did not react during the cooling stage of the solution annealing cycle. Figure 26 shows a high magnification view of the dual mode γ' formed in the dendritic core regions. The γ' has been etched away leaving empty sites.

The final result of the FHT is a more homogeneous structure than in the as cast condition, although variations still exist between interdendritic an dendritic core regions (Figure 25A). The γ' comprises a bimodal distribution of primary cuboidal precipitates together with secondary spheroidal precipitates. Isolated areas of large eutectic γ' may also be present. The large script and blocky MC carbides remain in the interdendritic regions, both at intergranular and transgranular sites, and a fine distribution of smaller $M_{23}C_6$ carbides particles occupies intergranular spaces.

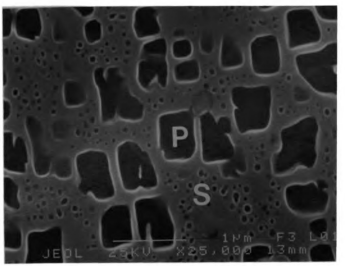

FIGURE 26- DUAL MODE γ' IN THE SOLUTION + AGE CONDITION
(Reagent # 5 / P- Primary γ'sites, S- Secondary γ'sites)

Due to the relatively short time involved in the heat treating cycles and the anchoring effect of the intergranular MC and $M_{23}C_6$ carbides, there is no significant grain growth. The final grain size as measured by the intercept technique remained to be ASTM No. 2.4.

6.3.2 **Microstructural Evaluation of Weld Deposits**

As it was shown in Figure 9, the buildup process created a uniform layer appearance with good interlayer bonding. The microstructure of the weld deposit consisted of irregular shaped grains, ASTM size 4.5, delineated by a high carbide concentration (Figure 27).

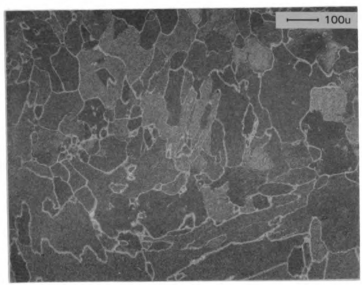

FIGURE 27- GRAIN STRUCTURE OF AS WELD DEPOSIT
(Reagent # 1)

The solidification morphology was identified as columnar dendritic, which is characterized by the growth of pockets of dendrites along basically the same direction (**54**). As it is shown in Figure 28, these essentially parallel dendrites combine to form one grain with a well developed substructure. Some weld porosity is also present. Figure 29 presents the same structure at higher magnification, which shows very limited branches off the main dendrite arms. The mean primary arm spacing was found to be 8.1 μm.

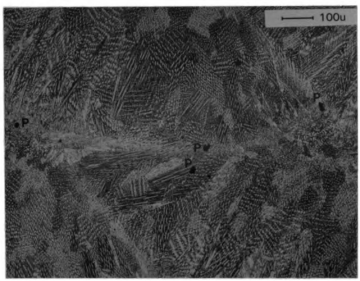

FIGURE 28- GRAIN SUBSTRUCTURE OF AS WELD DEPOSIT
(Reagent # 2 / P-Porosity)

FIGURE 29- DENDRITIC STRUCTURE OF AS WELD DEPOSIT
(Reagent # 2)

The smaller grain size and dendrite arm spacing, as compared with the cast microstructure, is the result of the higher cooling rate and the associated large undercooling. This condition increases the nucleation rate and reduces the diffusion distances, leading to a finer and more homogeneous structure.

Observations at high magnification (Figures 30 and 31) revealed that the grains were delineated by discrete spheroidal precipitates as in the cast structure. However, inside the grains, the dendritic core regions showed a solid solution of γ phase with no γ' precipitates, and the interdendritic regions showed a uniform distribution of small spheroidal carbide precipitates.

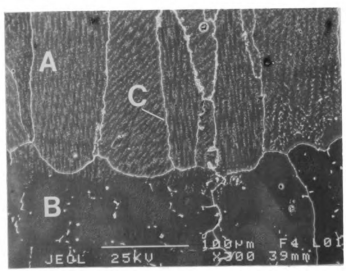

FIGURE 30- GENERAL CARBIDE DISTRIBUTION IN WELD DEPOSIT (Reagent # 6 / A-Weld Deposit, B-Base Material, C-Weld Deposit Grain Boundaries)

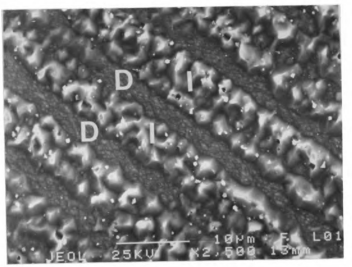

FIGURE 31- DISTRIBUTION OF CARBIDES IN THE DENDRITIC STRUCTURE OF AS WELD DEPOSIT
(Reagent # 6 / D- Dendritic Core Regions, I- Interdendritic Regions)

EDX analyses showed the grain boundary precipitates to be Cr-rich $M_{23}C_6$ carbides and the interdendritic precipitates to be Ti/Ta-rich MC carbides, with compositions equivalent to those presented in Figure 24. The size and morphology of the interdendritic carbide particles showed variations between two specific regions (Figure 32). A band of approximately 15 μm along the fusion line contained small feather-type particles of approximately 2 μm in diameter, while the rest of the deposit contained small spheroidal-type particles of approximately 0.5 μm in diameter. Both types of carbides are shown in Figure 33.

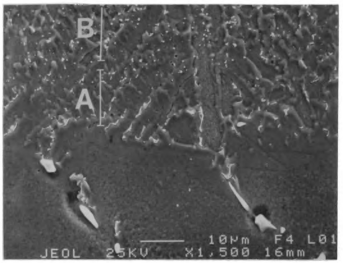

FIGURE 32- CARBIDES DISTRIBUTION ALONG FUSION LINE
(Reagent # 6 / A-Feather-type Carbide Region,
B-Spheroidal-type Carbide Region)

According to the above observations, there are significant differences between the as cast structure and the weld structure. Table 14 presents the characteristic features of both microstructures.

TABLE 14- MAIN MICROSTRUCTURAL CHARACTERISTICS OF AS CAST AND AS WELD CONDITIONS

FEATURE	AS CAST STRUCTURE	AS WELD STRUCTURE
Grain Size	ASTM 2.4	ASTM 4.5
Solidification Morphology	Equiaxed Dendritic	Columnar Dendritic
Mean Primary Arm Spacing	93.0 μm	8.1 μm
Phases	γ' (Eutectic, Prim., Second.) Script MC Blocky MC Spherical $M_{23}C_6$	No γ' Fine Dendritic MC Superfine Cellular MC Spherical $M_{23}C_6$

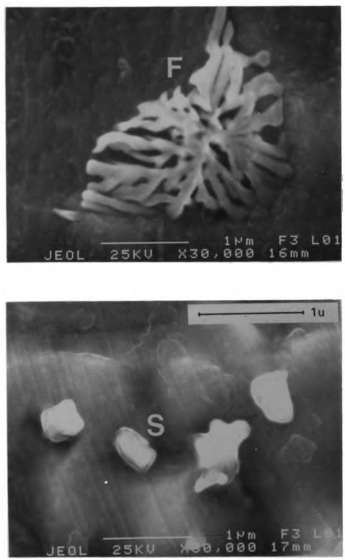

FIGURE 33- MORPHOLOGY OF CARBIDES IN THE WELD DEPOSIT (Reagent # 6 / F- Feather-type Carbide, S- Spheroidal-type Carbide)

It is important to point out that a previous study on the effects of solidification conditions on MC carbides in IN-738LC (**40**), indicated that the size and morphology of MC carbides depend on the cooling rate. In particular, the transition between fine dendritic or small feather-shape morphology and the superfine cellular or small spheroidal-shape morphology is around 1.1 x 10^5 K/s. Therefore, it can be established that the cooling rate at the fusion line of the weld pool must have been approximately 1 X 10^5 K/s.

Finally, it should be mentioned that the deposition of subsequent layers of filler material did not show any significant changes in the microstructure of the weld deposit. This may be explained by the fact that even though each additional weld pass produces a high temperature thermal gradient in the layer beneath, its time duration is extremely brief, so that no phase transformations occur. Also, because of the low heat input of the process, each additional pass was deposited over material that had been cooled to nearly room temperature, and this caused the solidification cooling rate to be approximately constant for each pass. This result is supported by temperature readings taken with a contact pyrometer on the weld deposits immediately after the lay down of the last pass, which indicated a surface temperature of 427 K.

6.3.3 **Microstructural Evaluation of Fusion Zone**

Metallographic observations showed a well defined fusion line, with a drastic change in the microstructure across it. Since the weld pool is formed on melted regions of the base metal, and the filler material has the same chemistry as the substrate, initial solidification tends to occur by epitaxial growth as shown in Figure 34.

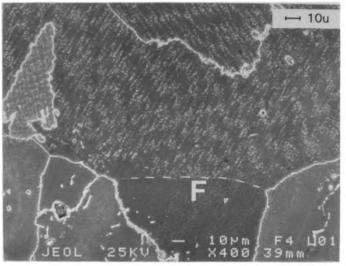

FIGURE 34- GENERAL MICROSTRUCTURE AT THE FUSION LINE
(Reagent # 6 / F- Fusion Line)

Figure 35 shows the dissolution of the phases in the weld deposit. The fine dendritic and superfine cellular MC carbides are not resolved because of their small size. This micrograph also shows how large script-type MC carbide precipitates remain present in the weld deposit at the immediate vicinity of the fusion line. This is the result of their high temperature stability. However, they are dissolved as they get further inside the weld pool. It should be pointed out that a previous study, this time on the effects of melting temperatures on the cast structure of IN-738LC (**20**), indicated that a temperature above 1868 K is required for the dissolution of primary carbides. Since the base metal primary carbides are eventually dissolved at a short distance from the fusion line, it can be established that the weld pool reached at least 1868 K during the deposition welding experiment (the liquidus temperature of alloy IN-738LC is 1590 K).

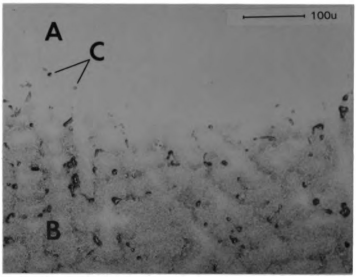

FIGURE 35- DISSOLUTION OF PHASES AT THE FUSION LINE
(Reagent #2 / A- Weld Deposit, B- Base Material,
C- Retained MC Carbides)

Figure 36 presents a high magnification view of the fusion zone, which shows a sharp dissolution of small cubic γ', a progressive dissolution of a large block of eutectic-γ', the fine dendritic MC carbides in the weld deposit and a script-shape carbide embedded in the weld deposit. If the heat affected zone (HAZ) is defined to be the distance required for a complete dissolution of the eutectic-γ', then from Figure 36, it is estimated that the HAZ has an approximate size of 7 μm.

A final important characteristic observed in the fusion zone is the incipient melting of the base material along the grain boundaries, as shown in Figure 37. Its occurrence is explained by the fact that the grain boundaries are located at interdendritic regions, where the last fraction of the melt freezes. The high solute concentration produced by segregation causes a drop in the melting temperature of this region, with respect to the rest of the material. Consequently, there is partial melting of the base material beyond the fusion line, along the grain boundaries.

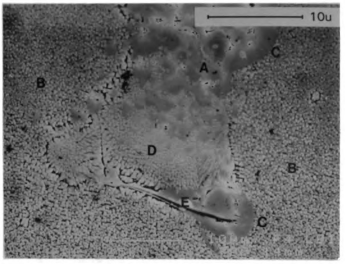

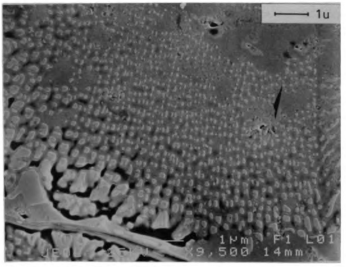

Detail of Area D

FIGURE 36- MICROSTRUCTURE AT THE HAZ
(Reagent # 4 / A- Weld Deposit, B- Base material, C- Dissolution of Cubic γ', D- Dissolution of Eutectic-γ', E- Script MC Carbide)

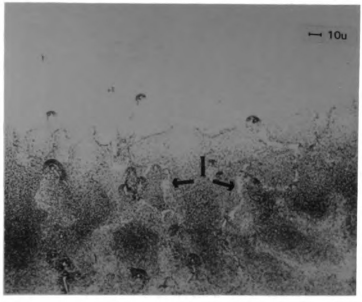

FIGURE 37- INCIPIENT MELTING IN HAZ
(Reagent #2 / I- Incipient Melting at Grain Boundaries)

6.3.4- **Evaluation of Discontinuities**

For the purpose of determining the effect of the base metal condition on the quality of the weld deposits, microscopic observations were carried out on the fusion zone of weld coupons manufactured with substrate material in each of the three pre-weld heat treated conditions.

Two distinctive types of linear indications were detected, both originating in the base metal in the immediate vicinity of the fusion line. These will be referred to as type A and type B linear indications.

Type A Linear Indications

This type of indication was determined to be intergranularly propagated cracks, associated to incipient melting in the interdendritic regions. In some cases this cracks extended into the weld material. Figure 38 shows a view of one of the cracks. Figure 39, which corresponds to a sample with a different etching treatment, shows another crack running along a grain boundary that was partially melted. Figure 40 shows an SEM view of other cracks of this type along the interdendritic spaces. Carbides which were not dissolved during incipient melting appear trapped inside the cracks.

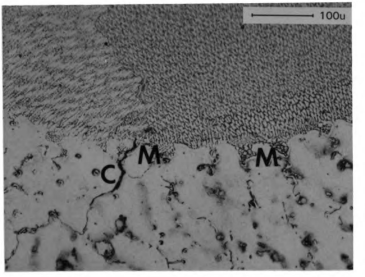

FIGURE 38- TYPE A LINEAR INDICATION
(Reagent #1 / C- Crack, M- Areas of Incipient Melting)

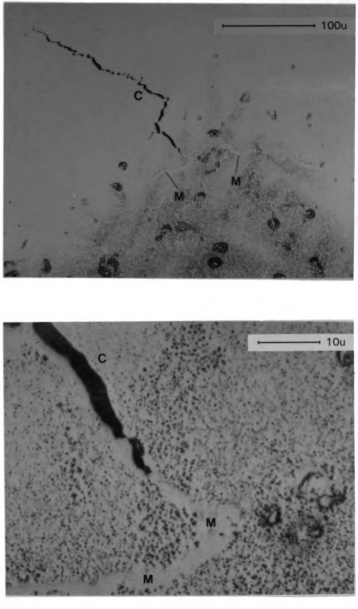

FIGURE 39- CRACK PROPAGATED INTO WELD DEPOSIT
(Reagent #2 / C- Crack, M- Areas of Incipient Melting,
lower micrograph shows detail of origin of crack)

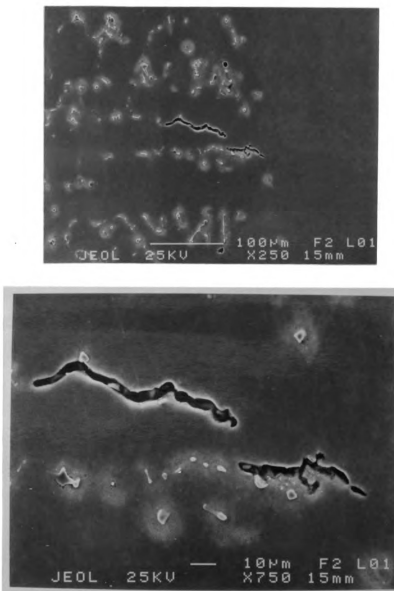

FIGURE 40- CRACKS IN INTERDENDRITIC REGIONS
(Reagent #6 / Lower micrograph shows detail of cracks)

ge
wh
cra

me
bas

inte
cont
clos
were
durin
mate

coupo
the ra
creati
weld

IN-738
was no

As it was indicated in section 2.3.2, cracking of Ni-base superalloys is generally associated either to age hardening through reprecipitation of γ' in the HAZ, which causes strain age cracking, or constitutional liquation which causes liquation cracking.

The characteristics of the type A cracking indicate that they are formed by the mechanism of liquation cracking, due to the coring type segregation present in the cast base material.

Type B Linear Indications

The second type of linear indications were also found to be related to interdendritic regions, as shown in Figure 41. Inside the base material they appear as a continuous flaw-line; however, in the weld deposit they appeared as lines of very closely spaced porosity. Detailed observations of the flaw-line section reveal that they were elongated interdendritic shrinkage cavities formed along the interdendritic regions during the casting process of the base material. Figure 42 shows an area inside the base material containing globular and elongated shrinkage cavities.

When the casting defects shown in Figure 42 are close to the surface of the coupon being welded, the molten pool entraps parts of these shrinkage cavities. Due to the rapid solidification process, there is no time for the gas to travel to the surface, creating what appears to be a crack line that extends from the base material into the weld deposit.

Since the type B linear indication is not directly related to the response of alloy IN-738LC to the laser beam welding process, but to a pre-existing casting defect, it was not taken into account in the quantification of indications presented below.

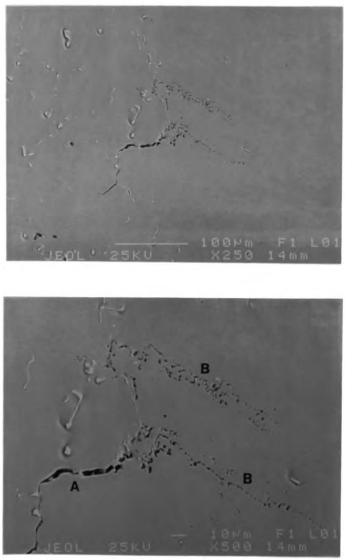

FIGURE 41- TYPE B LINEAR INDICATION AT TWO DIFFERENT MAGNIFICATIONS
(Reagent #6 / A- Continuous Flaw-line, B-Porosity Line)

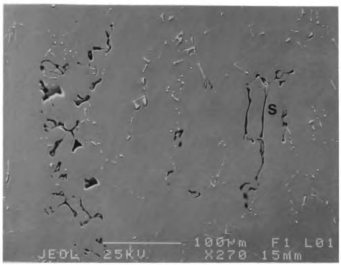

FIGURE 42- CASTING DEFECTS IN THE BASE METAL
(Reagent #6 / S- Elongated Shrinkage Cavity)

To minimize the formation of type B linear indications, the welding process would have to be carried out on hipped cast material, which contains a lesser amount of casting porosity and shrinkage cavities.

Quantification of Indications

In order to establish a comparison between the susceptibility to cracking for the three pre-weld conditions, the total length and count of indications was determined through observations in the optical microscope (50-400X). Due to the small size of the indications, which ranged from 0.04 to 0.60 mm long, and interference with the script carbides, it was not possible to carry out an automatic counting in the image analyzer.

Tables 15 and 16 show the results of this quantification and the indication density, as related to the total length of fusion line inspected.

TABLE 15- QUANTIFICATION OF LINEAR DISCONTINUITIES FOR THE PRE-WELD CONDITIONS

PRE-WELD CONDITION	COUNTS	TOTAL INDICATION LENGTH (mm)	AVG. LENGTH (mm)	STD. DEV. (mm)	TOTAL LENGTH INSPECTED (mm)
AS CAST	15	3.60	0.24	0.161	73.5
SOL.	3	0.75	0.25	N.A.	73.5
SOL. + AGE	6	1.32	0.22	0.071	73.5

TABLE 16- INDICATION DENSITY FOR THE PRE-WELD CONDITIONS

PRE-WELD CONDITION	INDICATION COUNT DENSITY (counts/mm)	INDICATION LENGTH DENSITY (mm/mm)
AS CAST	0.204	0.049
SOL.	0.041	0.010
SOL. + AGE	0.082	0.018

The results presented in Table 15 indicate that the solution condition yields both the least amount of cracks and the shortest length of cracks per millimeter of weld deposit. The FHT condition results are close to those of the solution condition. The as cast results, on the other hand, show a significantly greater discontinuities density than the other two conditions.

As discussed in Section 2.3.2, the better response of the solution condition is related to two factors:

1. The homogenization effect obtained during the solution treatment, which increases the incipient melting temperature at interdendritic regions.

2. The lower strength and higher ductility of the material in this condition, which allows it to better accommodate the strains originating from thermal stresses.

6.4- POST-WELD HEAT TREATMENT EFFECTS ON LASER DEPOSITION WELDS

Two PWHT were evaluated in this research: 1) the complete processing treatment, which consists of HIP to minimize the amount of cast discontinuities, followed by solution and aging to precipitate the hardening phase, and 2) the standard hardening heat treatment, which consists only of the solution and aging cycles.

The effect of HIP on the welding discontinuities will be presented first, and then the microstructures obtained after the PWHT in both the deposition welds and the base material.

6.4.1 Effects of Hot Isostatic Pressing

Figure 43 shows perpendicular sections of laser deposition welds before and after HIPing. The HIPed samples showed a significant decrease in the amount of indications, both linear and spherical. In order to quantify the healing effect, the amount and sizes of both types of discontinuities were measured.

As in the case of the quantification of indications for the Welding Procedure Qualification (Section 6.2.2), the amount, size and area fraction of the spherical indications were measured with the image analyzer; however, the measurements were carried out at a magnification of 50X instead of 7.5X. On the other hand, as in the case of the quantification of indications for the pre-weld conditions (Section 6.3.4), the length of the linear indications was determined by optical measurements through the light microscope (50-400X).

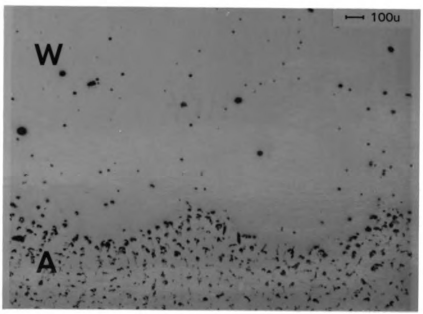

BEFORE HIP

AFTER HIP

FIGURE 43- CROSS SECTIONS VIEWS BEFORE AND AFTER HIP

(Unetch / A-base Material, W- Weld Deposit)

Spherical Indications

The image analyzer was capable of detecting indications larger than 2.5 μm. The porosity section sizes were classified into 15 size ranges, and the Method of Saltykov was used to convert these values into the actual size distribution.

Specifically, the Saltykov Method allows one to estimate the size distribution of particles in unit volume of an aggregate, from measurements made on a planar microstructure. It is based on a study of the probability of a random plane intersecting a sphere at a certain section size (**55**).

Tables 17 and 18 present the porosity size distribution before and after HIP, respectively, based on measurements over 10 cross sections for each condition. Figure 44 shows these results in a graphical form.

TABLE 17- POROSITY SIZE DISTRIBUTION BEFORE HIP

SIZE RANGE ($x10^{-3}$ mm)	COUNT DENSITY (counts/mm^2)	STANDARD DEVIATION	VOLUME DISTRIBUTION (counts/mm^3)
0-5	11.56	7.27	1815.59
5-10	12.44	3.85	992.99
10-15	11.94	4.54	826.31
15-20	7.26	3.54	433.66
20-25	3.79	3.17	199.34
25-30	1.77	0.72	74.02
30-35	1.26	1.03	57.87
35-40	0.32	0.45	1.61
40-45	0.57	0.70	18.26
45-50	0.38	0.33	11.73
50-55	0.19	0.43	2.01
55-60	0.32	0.54	10.54
60-65	0.13	0.27	3.74
65-70	0.06	0.20	1.48
70-75	0.06	0.20	2.35

TABLE 18- POROSITY SIZE DISTRIBUTION AFTER HIP

SIZE RANGE ($x10^{-3}$ mm)	COUNT DENSITY (counts/mm^2)	STANDARD DEVIATION	VOLUME DISTRIBUTION (counts/mm^3)
0-5	5.87	1.93	1023.90
5-10	4.36	1.62	436.80
10-15	1.96	1.47	154.13
15-20	0.69	0.76	47.78
20-25	0.13	0.27	4.39
25-30	0.13	0.27	4.94
30-35	0.06	0.20	0.00
35-40	0.19	0.31	9.79
40-45	0.00	0.00	0.00
45-50	0.00	0.00	0.00
50-55	0.00	0.00	0.00
55-60	0.00	0.00	0.00
60-65	0.00	0.00	0.00
65-70	0.00	0.00	0.00
70-75	0.00	0.00	0.00

Figure 44 shows that the number of pores within each size range is considerably reduced, esspecially above 5μm, and the porosity density distribution is shifted towards the lower values (left). This behavior is consistent with the fact that porosity healing is due to mechanical collapsing (deformation) and diffusion; therefore, the pore size is gradually reduced until they are eliminated or they become stabilized by restraining action of internal gas pressure and oxidation.

An important observation is that the porosity area fraction, calculated to be 1.04 $x10^{-2}$ before HIP, is decreased to 8.91 x 10^{-4} after HIP with no pore exceeding 40 μm, which corresponds to a reduction factor of 11.8. A previous study on the removal of casting porosity in IN-738 (**56**), determined a decrease in porosity area fraction from 2 $x10^{-3}$ to 26 $x10^{-5}$ with no pore exceeding 50 μm, which corresponds to a reduction factor of 7.7. This result indicates that the response of the weld deposit to HIP is in the same order of magnitude as the response of cast material to the same treatment.

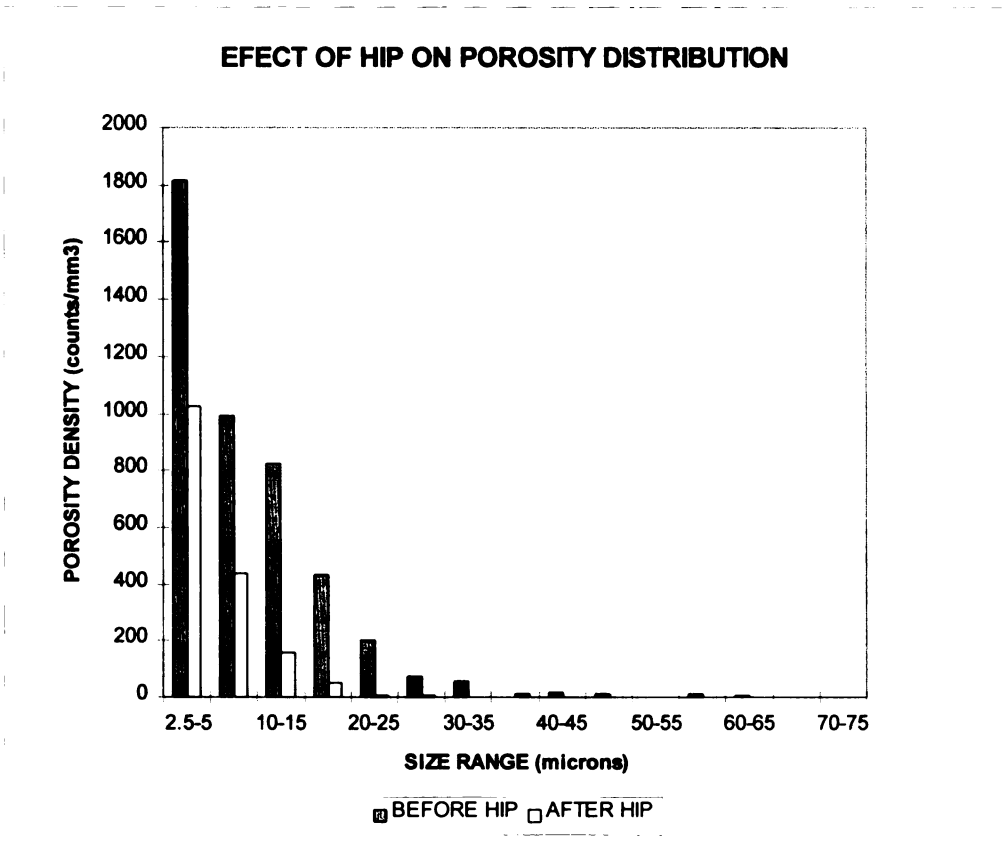

FIGURE 44- POROSITY SIZE DISTRIBUTION BEFORE AND AFTER HIP

Linear Indications

Table 19 shows the results of the optical measurements taken after HIP for each pre-weld condition. Table 20 compares the indication density values to those obtained in Section 6.3.4.

TABLE 19- QUANTIFICATION OF LINEAR INDICATIONS AFTER HIP

PRE-WELD CONDITION	TOTAL COUNTS	AVERAGE LENGTH (mm)	TOTAL LENGTH INSPECTED (mm)
AS CAST	2	0.11	31.5
SOL.	0	0	31.5
SOL. + AGE	1	0.12	31.5

TABLE 20- LINEAR INDICATIONS DENSITY BEFORE AND AFTER HIP

PRE-WELD CONDITION	COUNT DENSITY (counts/mm)		LENGTH DENSITY (mm/mm)	
	BEFORE HIP	AFTER HIP	BEFORE HIP	AFTER HIP
AS CAST	0.204	0.063	0.049	0.0035
SOL.	0.041	0	0.010	0
SOL. + AGE	0.082	0.032	0.018	0.0038

The indications density results show that HIP has also an important healing effect on the linear discontinuities. No similar values were found in the literature, that would allow a comparison to the healing of linear indications in cast material.

It should be mentioned that linear discontinuities of the sizes observed after HIP are not detectable by conventional non-destructive testing techniques; therefore, parts with such discontinuities would not be rejected by standard fabrication inspections. The safety factors included in the design of machinery parts take into account the possibility of their occurrence.

6.4.2- **Microstructural Evaluation**

As it was previously mentioned, the thermomechanical and heat treatments applied to superalloys are designed to give a proper balance between intergranular and

grain boundary strength. Inside the grains, this is achieved by providing solid solutioning strengthening to the matrix and controlling the size, shape, distribution and amount of γ'. The grain boundary strength is achieved by a proper distribution of carbides.

In order to determine the response of the laser weld deposit to the hardening heat treatment cycles, both the intragranular and intergranular microstructural features were evaluated, and compared with those of the heat treated base material. The size and amount of the γ' phase was quantified by using the image analyzer; while its shape and distribution, as well as the distribution of carbides at grain boundaries were qualitatively determined through SEM observations.

The quantification process was carried out by selectively etching the γ' in order to obtain proper contrast, as shown in Figure 26, and then determining the amount, size and area fraction of the voids.

Solution + Age Treatment

Figure 45 shows a general view of the microstructure, which reveals an inhomogeneous distribution of γ' between the interdendritic and dendritic core regions in the base material, and a homogeneous distribution in the weld deposit. The inhomogeneous distribution in the base material is the result of element segregation, as described in Section 6.3.1. The uniform precipitation in the weld deposit is the result of the higher solidification cooling rates during welding, which reduce the diffusion distances, as described in Section 6.3.2.

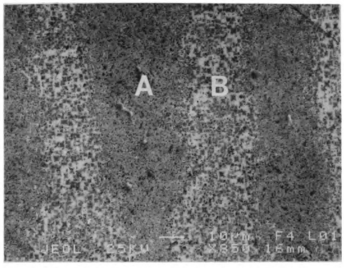

BASE MATERIAL

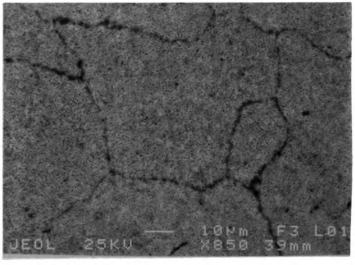

WELD DEPOSIT

FIGURE 45- GENERAL MICROSTRUCTURE OF SOLUTION + AGE SAMPLE
(Reagent #4 / A-Dendritic Core Region, B- Interdendritic Region)

Figure 46 shows a high magnification view of the microstructures of both the base material and the weld deposit. The base material shows a different size distribution between the interdendritic and dendritic core regions, while the weld deposit showed only one size distribution. In all cases, the γ' shows a bimodal type precipitation with large cubic primary particles and smaller spherical secondary particles.

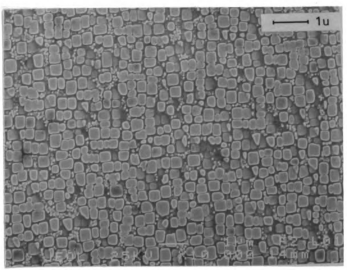

BASE MATERIAL
DENDRITIC REGION

FIGURE 46- γ' IN SOLUTION + AGE SAMPLE
(Reagent #4)

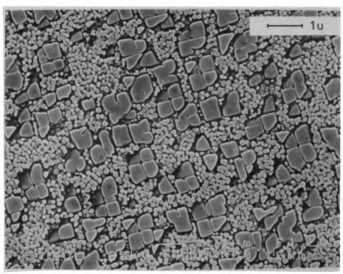

BASE MATERIAL
INTERDENDRITIC
REGION

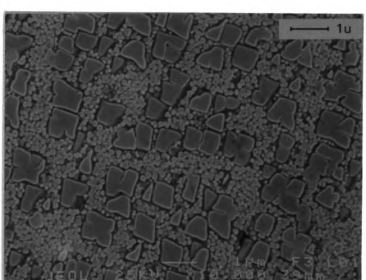

WELD DEPOSIT

FIGURE 46 (cont'd)

Figures 47 and 48 show the carbide distribution in the base material and the weld deposit, respectively. As it was mentioned in Section 6.3.1, the carbide size and distribution is not affected by the short time hardening treating cycles, but only by the long time service exposure at high temperatures. Therefore, the base material maintains a large concentration of large MC carbides at grain boundaries and a small concentration in the inner grain sites, as well as small discrete $M_{23}C_6$ carbides at grain boundaries. Similarly, the weld deposit maintains a fine dispersion of MC carbides throughout the microstructure, and small discreet $M_{23}C_6$ carbides at the grain boundaries.

It is important to note that the presence of highly stable MC carbides in the grain boundaries ensures grain boundary strength at high temperature. Consequently, the small concentration of MC carbides in the weld deposit grain boundaries will produce lower creep properties as compared with the base material.

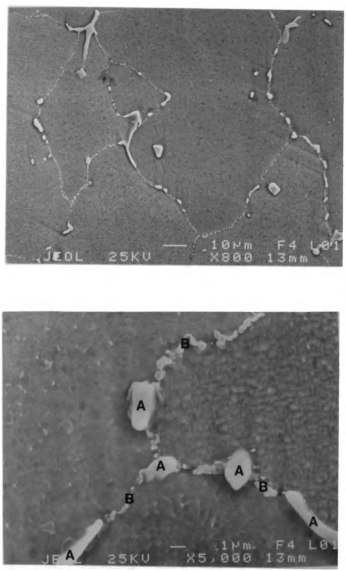

FIGURE 47- CARBIDE DISTRIBUTION IN BASE MATERIAL FOR SOLUTION + AGE SAMPLE
(Reagent #6 / Detail of grain boundary is shown in lower micrograph, A- MC Carbides, B- $M_{23}C_6$ Carbides)

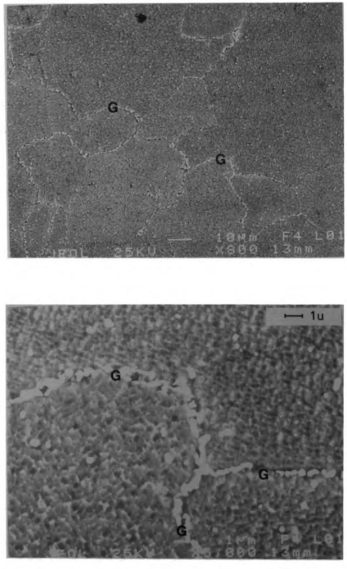

FIGURE 48- CARBIDE DISTRIBUTION FOR WELD DEPOSIT IN SOLUTION + AGE SAMPLE
(Reagent #6 / Lower micrograph shows detail of grain boundary, G- $M_{23}C_6$ Carbides at Grain Boundary

HIP + Solution + Age

The HIP cycle previous to the hardening heat treatment produces an additional homogenization of the γ' phase in the base material, and it does not produce any significant changes in the weld deposit. Figure 49 shows a general view of the base material microstructure, which reveals a more uniform distribution than that of Figure 45. Figure 50 shows higher magnification views of the bimodal γ' distribution in the weld material and the weld deposit, respectively. Figure 51 shows a detailed view of the γ' bimodal distribution, consisting of large cubic primary particles and smaller spherical secondary particles.

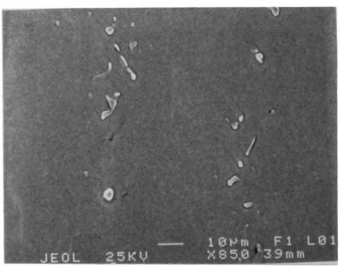

FIGURE 49- GENERAL MICROSTRUCTURE OF HIP + SOLUTION + AGE BASE MATERIAL SAMPLE
(Reagent #4)

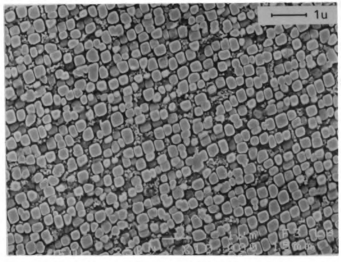

BASE MATERIAL
DENDRITIC REGION

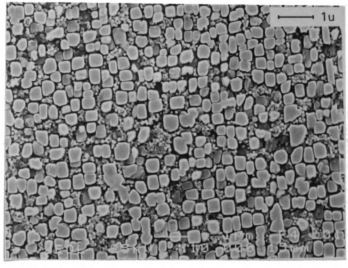

BASE MATERIAL
INTERDENDRITIC
REGION

FIGURE 50- γ' IN HIP + SOLUTION + AGE SAMPLE
(Reagent # 4)

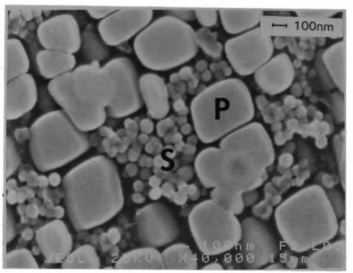

WELD DEPOSIT

FIGURE 50 (cont'd)

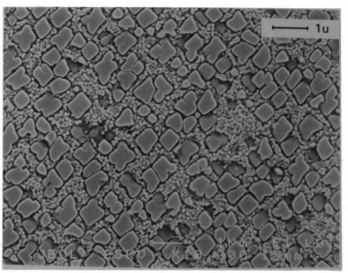

FIGURE 51- DETAIL OF BIMODAL DISTRIBUTION IN WELD DEPOSIT
(Reagent #4 / P- Primary γ', S- Secondary γ')

6.4.3- γ' Size Determination

The primary γ' size was determined by the Method of Weibel and Gomez (**57**). The method relates the particles count density (counts/μm^2), the particles area fraction ($\mu m^2/\mu m^2$) which is equivalent to volume fraction, and the stereological coefficient β, to the characteristic dimension a (cube side). The first two values were determined by the image analyzer, while the coefficient β, which is a dimensionless value related to the shape of the particle considered, was found in the literature (**57**).

This method requires the particles to have a well defined shape and equal size. The first condition is approximated by considering the particles to be perfect cubes ($\beta = 1.84$), and the second condition is basically satisfied by restricting the measurements to regions of approximately uniform size distribution (interdendritic or dendritic core regions). The calculations were based on a sample of at least 500 particles per region.

The secondary γ' was measured directly on high magnification micrographs, as on Figure 51. The sampling was limited to 25 particles, due to the difficulty in obtaining a good resolution in micrographs at high magnifications.

Table 21 shows the calculated primary γ' size and Table 22 shows the measured secondary γ' size.

A literature review on the fabrication and processing of cast IN-738LC alloy revealed a range of acceptable γ' sizes and volume fractions for the two PWHT considered in this research. In all cases the reported values corresponded to material that complied with the mechanical properties required in the commercial specification of the alloy. Table 23 shows these values.

TABLE 21- PRIMARY γ' SIZE

CONDITION	REGION	AREA ANALYZED (μm^2)	COUNTS	COUNT DENSITY ($\#/\mu m^2$)	AREA FRACTION	CUBE SIDE (μm)
S+A	BASE METAL:					
	INTERDENDRIT.	283.796	501	1.765	0.392	0.578
	DENDRITIC	141.898	538	3.791	0.345	0.370
	WELD DEPOSIT	141.898	510	3.594	0.385	0.401
H+S+A	BASE METAL:					
	INTERDENDRIT.	275.306	537	1.951	0.361	0.527
	DENDRITIC	274.829	596	2.169	0.389	0.519
	WELD DEPOSIT	264.472	625	2.363	0.388	0.497

TABLE 22- SECONDARY γ' SIZE

REGION	MEAN DIAMETER (μm)	STD. DEV.
BASE MATERIAL	0.115	0.0035
WELD DEPOSIT	0.111	0.0057

TABLE 23- γ' SIZE AND VOLUME FRACTION REPORTED IN THE LITERATURE

CONDITION	REFERENCE	COARSE γ' (μm)	FINE γ' (μm)	γ' VOL. FRACTION
SOL + AGE	25	0.35	0.10	0.30
	26	0.40-0.42	0.073-0.084	0.40
	46	0.58	0.14	0.43
	58	0.37-0.64	0.10	---
	59	0.45	0.10	---
	RANGE:	0.35-0.64	0.073-0.14	---
HIP + SOL + AGE	60	0.60	0.10	---
	59	0.38-0.60	0.10	---
	RANGE:	0.38-0.60	0.10	---

Previous studies have proven a direct correlation between strengthening of superalloys and the γ' size. The materials room temperature tensile strength and hardness increase linearly as the primary γ' coarsens from precipitation to a particle size of approximately 0.5 μm (age hardening peak); then, linearly decreases as the primary γ' grows beyond this value. The acceptable γ' size range reported in the literature (Table 23), is around this age hardening peak value. As it was mentioned in Section 2.1, initially the operative strengthening mechanism involves cutting of the γ' particles by dislocations, and strength increases with γ' size. After the age hardening peak is reached, strength decreases with continuing particle growth because dislocations no longer cut γ' particles but bypass them.

By comparing the γ' sizes and volume fraction presented in Tables 20 and 21 with those in Table 22, it is observed that the values obtained in this research agree with those of a properly age hardened material.

6.5- **HARDNESS MEASUREMENTS**

Figures 52 and 53 show the microhardness variation across the fusion line after the solution + age and the HIP + solution + age PWHT, respectively. Distance values increase in the direction of the weld deposit. Each case includes the three base material conditions evaluated in Section 6.3.

As it can be seen in the graphs, the hardness values show no significant variation across the fusion line, where the values were found to be around 455 Hv,

with a standard deviation of 11 Hv. Additionally to the measurement error, the small variations observed are believed to be related to the presence of localized clusters of MC carbides in the interdendritic spaces and to areas of vary small grain size in the weld deposit, which increase the hardness; as well as to the presence of porosity in both the base and weld deposit materials, which decrease the hardness.

The literature reports hardness values in the range of 430 to 485 Hv for IN-738LC alloy in the full heat treated condition (**25, 29, 61, 62**). Therefore, the experimental values are in agreement with the hardness values expected from a properly heat treated alloy.

FIGURE 52- MICROHARDNESS MEASUREMENTS FOR SOLUTION + AGE PWHT

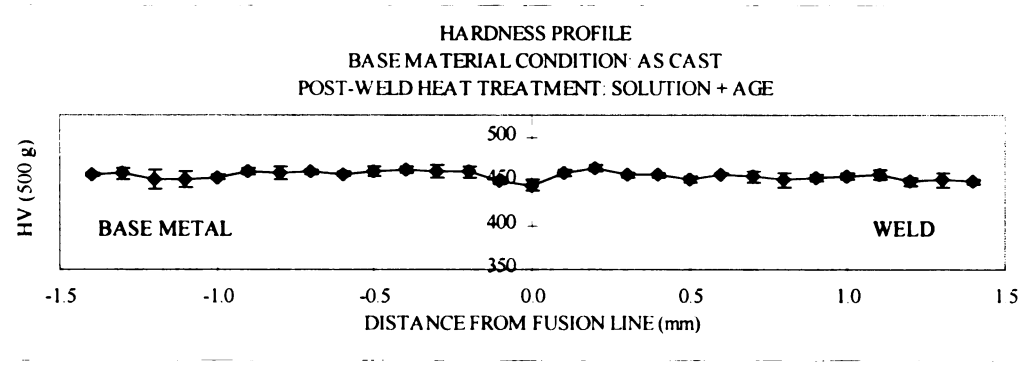

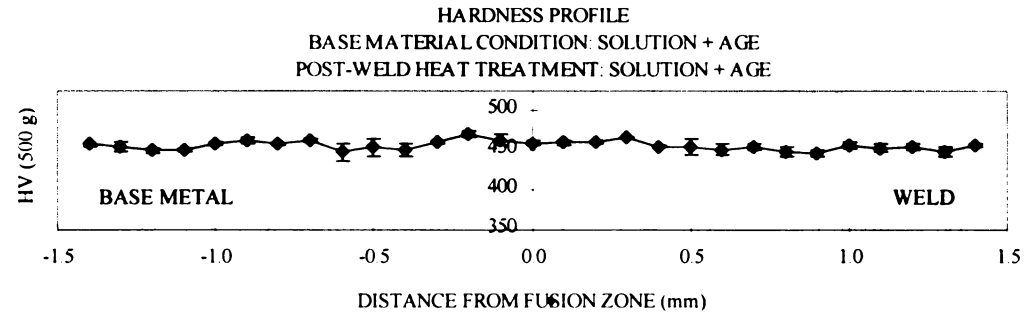

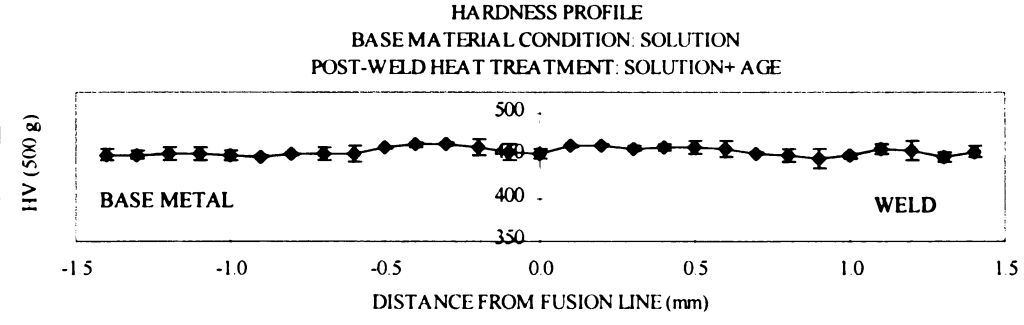

FIGURE 53- MICROHARDNESS MEASUREMENTS FOR HIP + SOLUTION + AGE PWHT

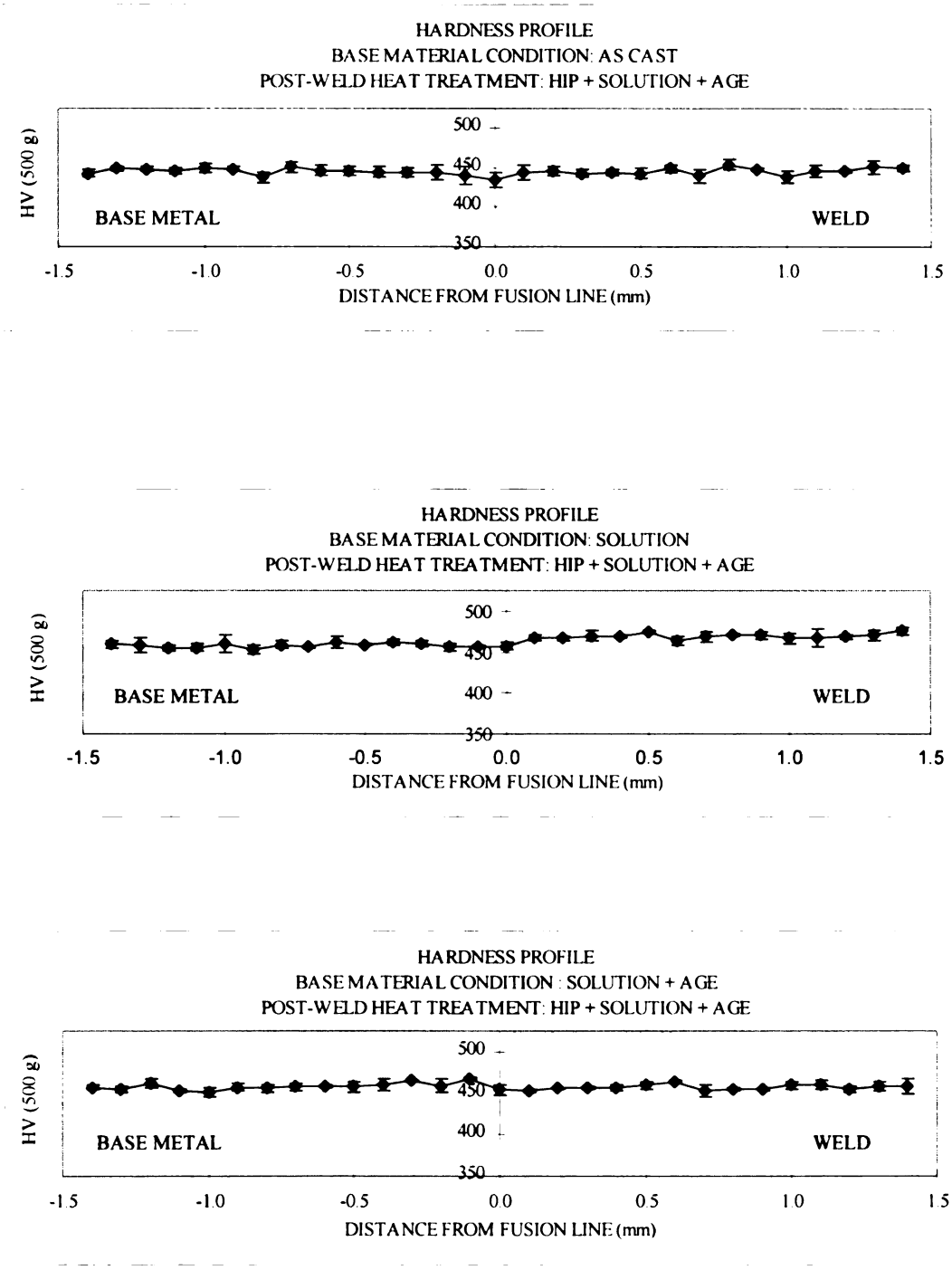

CHAPTER 7

SUMMARY OF RESULTS

In the first part of this research, a set of parameters was defined that produced a minimum amount of linear discontinuities in the weld deposit (0.165 counts/mm^2 for the spherical, and 0.029 counts/mm^2 for the linear indications, with a sensitivity of 0.07 mm and 0.21 mm, respectively). This set of parameters corresponded to that yielding the lowest heat input, while still producing a well fused deposit. Additionally, a quantitative chemical analysis showed no significant composition variation between the powder filler material and the weld deposits, which indicated that there was no significant vaporization of the alloy elements during the laser welding process.

In the second part of this research, the selected welding parameters were used to prepare deposition welds on base material in three different heat treated conditions (as cast, solutionlized, solutionize + age). Metallographic and EDX analyses showed significant differences between the substrate in the pre-weld condition and in the as weld deposit.

The substrate showed a large grain size (ASTM 2.4) with equiaxed dendrites (93.0 μm mean primary arm spacing), and a large variation in the precipitate size and morphology. The inner grains showed γ' in eutectic lamellae, cubic and spherical morphologies, as well as MC carbides in blocky and script morphologies. The grain boundaries were delineated by script MC and spheroidal $M_{23}C_6$ carbides. EDX x-ray mapping revealed a high concentration of Ta, Ti, Nb and Zr in the interdendritic regions, which is in agreement with the previously determined distribution coefficients, k, for alloy IN-738LC. This element segregation caused a larger concentration of carbides and eutectic γ' in the interdendritic regions, than in the dendritic core regions.

The weld deposit on the other hand, as a result of the rapid solidification, showed a more homogeneous structure composed of small grains (ASTM 4.5) with a columnar dendritic substructure (8.1 μm mean primary arm spacing). The γ' phase did not precipitate, and the MC carbides did not show large script or blocky morphology, but showed fine dendritic and cellular morphologies, with a uniform distribution in the interdendritic regions.

A morphology change in the MC carbides from fine dendritic to superfine cellular in the vicinity of the fusion line, indicated that the cooling rate was about $1x10^5$ K/s. Another important feature of the weld deposit was that the application of subsequent layers of filler material to form the multipass build-up did not cause any significant changes in the microstructure of the layers beneath. This is explained by the brief duration of the thermal gradient, which did not allow any phase transformation to take place.

Metallographic observations in the fusion line revealed discontinuities associated with the liquation cracking mechanism. Quantification of these discontinuities showed that the solution annealed base metal condition has the lowest susceptibility to this phenomenon (0.041 vs. 0.082 for the solutionized + age and 0.204 counts/mm for the as cast conditions). The reason for this lower susceptibility to cracking is the higher incipient melting temperature produced by homogenization at the solution annealing temperature, and the lower strength and higher ductility of the solutionized condition as compared with the aged condition, which allows better accommodation of the strains originating from thermal stresses.

The study of the effect of PWHT on the deposition welds, showed that HIPing has an important healing effect on both spherical and linear discontinuities. It reduced the porosity area fraction by a factor of 11.8, and eliminated all linear indications in

the weld coupons prepared on solution annealed base material, which already had the lowest indication density.

The final weld deposit and base material microstructures obtained after the solutionized + aged, and the HIP + solutionized+ aged PWHT, showed no significant changes in either the grain size or the carbide distribution, as compared with the original microstructures. Consequently, the weld deposits had a smaller grain size and a considerably smaller amount of MC carbides in the grain boundaries than the base material. However, both the weld deposit and the base material showed a bimodal distribution of γ' in sizes and volume fractions that corresponded to those of a properly aged hardened material.

The different grain size and carbide distribution in the weld deposit, as compared with the cast material, is expected to produce a negative effect on the creep properties. The fine grain size produces a larger grain surface for sliding to take place, and the absence of large blocky or script MC carbides facilitates the sliding process, especially above 1273 K, which corresponds to the $M_{23}C_6$ carbide solvus temperature.

The size, shape, distribution and amount of γ' in the inner grains of the heat treated weld deposit is expected to produce low temperature tensile properties equivalent to those of the heat treated cast material. This is supported by the microhardness values, which were found to be in the range given in the literature for a properly precipitation hardened IN-738LC alloy.

CHAPTER 8

CONCLUSIONS

- The laser beam powder welding process, under the parameters applied in this research, do not produce a detectable variation in the bulk composition of the IN-738LC weld deposit, as far as the sensetivity limits of chemical analysis by the inductively coupled plasma technique (+/- 0.05 wt %).

- Alloy IN-738LC base material in the solution annealed condition shows a lower susceptibility to liquation cracking than it does in the as cast and the solution + age conditions, when subjected to the laser beam powder welding process.

- The better response of the solution annealed base material is attributed with the homogenization effect obtained during the solution treatment, which increases the incipient melting temperature at interdendritic regions. It is also associated with the lower strength and higher ductility obtained by the reduction in the γ' size, which allows it to better accommodate the strains originating from thermal stresses.

- Hot Isostatic Pressing has a significant healing effect on the spherical and linear indications present in the laser beam weld deposits. It reduces the porosity area fraction by a factor of 11.8, and eliminates the linear indications in the fusion line of the solution annealed base material.

- The age hardened laser weld deposits showed a smaller grain size and a lesser amount of grain boundary MC carbides than the age hardened cast material; therefore, it is expected to have lower creep resistance. On the other hand, the age hardened laser weld deposit showed a size, shape, distribution and amount of γ' equivalent to that of a properly precipitation hardened cast material; therefore, it is expected to have adequate low temperature tensile properties.

BIBLIOGRAPHY

BIBLIOGRAPHY

1. Deblon, B., Keienburg, K., Kraftwerk Union AG "Refurbishing Gas Turbine Blades, Technical and Economical Aspects", Turbomachinery International, October 1985, pp 28-33.

2. Stringer, J., Viswanathan, R., "Life Assessment Techniques and Coating Evaluations for Combustion Turbine Blades", Conference Proceedings, Life Assessment & Repair Technology for Combustion Turbine Hot Section Components, Phoenix, AZ, 1990, pp 1-18.

3. Malone, G. "An Integrated Approach to Remanufacturing Turbine Blades", Welding Journal, June 1989, pp 20-26.

4. Esser, W., Deblon, B., Czech, N., "Refurbishment of Gas Turbine Blades - Concept, Development and Experience", Conference Proceedings, Life Assessment & Repair Technology for Combustion Turbine Hot Section Components, Phoenix, AZ, 1990, pp 313-322.

5. Cieslak, M., Stephens, J., Carr, M., "A Study of the Weldability and Weld Related Microstructure of Cabot Alloy 214", Metallurgical Transactions, Vol 19A, March 1988, pp 657-667.

6. Wetter, L., Albright, C., Jones, W., "Development of a Weldability Test for Pulsed Laser Beam Welding", Welding Research Supplement, Welding Journal, March 1986, pp 51-s - 62-s

7. McCay, M., Womack, M., McCay, D., Dahotre, N., "The Effect of Laser Pulse Tailored Welding on Inconel 718", ICALEO, 1990, pp 325-342.

8. Harrison, R., "Laser Powder Welding", Turbomachinery International, Sept.-Oct. 1994.

9. Basics of Laser Materials Processing, Grigoryants, A., Mir Publishers, Moscow,1994, pp 9-47, 69-116 and 195-226.

10. Eβer, W., McLean, M., Schneider, K., "Effect of Fabrication and Repair Procedures on the Performance of IN738 LC and IN 939", High Temperature Alloys for Gas Turbines and Other Applications (proceedings of a conference held in Li'ege, Belgium), D. Reidel Pub. Co.,1986.

11. Baeslack III ,W., Ernst, S., Lippold ,J., "Heat-Affected Zone Liquation Cracking in a Cobalt-Free Low-expansion Superalloy", Journal of Materials Science Letters 7, 1988, pp 1204-1208.

12. Welding, Brazing and Soldering, ASM Handbook, ASM International, Vol 6,1993.

13. Schilke, P., Foster, A., Pepe, J., Beltran, A. "Advanced Materials Propel Progress in Land-Based Gas Turbines", Advanced Materials & Processes, April 1992, pp 22-30.

14. Dionoro, G., Memola, F., "Laser Welding of Inconel 600", SPIE Vol 1397 Eighth International Symposium on Gas Flow and Chemical Lasers, 1990, pp 783-786.

15. Mehta, P., Cooper, E., Miller, R., "Laser Welding - A Parametric Study on INCO718", International Conference of Applications of Lasers and Electrooptics ICALEO, Boston, 1984, pp 43-52.

16. Albright, C., Chiang, S., "High Speed Laser Welding Discontinuities", Proceedings of the 7th International Congress on Applications of Lasers and Electrooptics ICALEO '88, October - November 1988, Santa Clara, pp 207-213.

17. Richards, N., Huang, X., Chatuverdi, C., "Heat Affected Zone Cracking in Cast Inconel 718", Materials Characterization, 1992, pp 179-187.

18. Sims, C., "Non Metallic Materials for Gas Turbine Engines", Advanced Materials & Processes, June 1991, ASM International, Vol 139, pp 32-35.

19. Properties and Selection: Irons, Steels and High Performance Alloys, Metals Handbook, Vol 1, 10th Edition, ASM International, 1990.

20. Decker, R., "Strengthening Mechanisms in Ni-based Superalloys", Proceedings of Steel Strengthening Mechanisms Symposium, Zurich, May 1969, pp 1-24.

21. Superalloys II, Sims, C., Stoloff, N., Hagel, W., John Wiley and Sons Inc., New York, 1987, pp 61-131 and 495-516.

22. Bhowal, P., "Effects of Cooling Rate on γ' Morphology", Metallurgical Transactions A, June 1990, Vol 21A, pp 1709-1717.

23. Wilkinson, N., "Technological Considerations in the Forging of Superalloys Rotor Parts", Metals Technology, July 1977, pp 346-359.

24. Viswanathan, R., "Microstructural Degradation Phenomena and their Effects on Blade Integrity", Proceedings Conference of Life Assessment and Repair, EPRI, Phoenix, April 1990, pp 155-164.

25. Steven, R., Flewitt, P., "Microstructural Changes Which Occur During Isochronal Heat Treatment of the Nickel-Base Superalloy IN-738", Journal of Materials Science, Vol 13, 1978, pp 367-376.

26. McColvin, G., "The Effects of Thermal Treatments on the γ' Precipitate Morphology and Creep-rupture Properties of Nimocast Alloy 738", Metal Science , Vol 11, October 1977, pp 447-452.

27. Kattus, J., "Nonferrous Alloys", Aerospace Structural Metals Handbook, Battelle Laboratories, March 1984, Code 4217.

28. Stevens, R., Flewitt, P., "Intermediate Regenerative Heat Treatments for Extending the Creep Life of the Superalloy IN-738", Material Science and Engineering, Vol 50, 1981, pp 271-284.

29. Stevens, R., Flewitt, P., "The Effects of γ' Precipitate Coarsening During Isothermal Aging and Creep of the Nickel-Base Superalloy IN-738", Material Science and Engineering, Vol 37, 1979, pp 237-247.

30. Lasers A Survey of Their Performance and Applications, Brown, R., Business Books Limited, London, 1969, pp 72-86.

31. Energy-Beam Processing of Materials, Taniguchi, N., Oxford Series of Advanced Manufacturing, Clarendon Press, Oxford, 1989, pp 1-62.

32. Laser Welding: State of the Art, Mazumder, J., Conference Proceedings Symposium Lasers in Metallurgy, ed. Mukherjee, K. and Mazumder, J., Metallurgical Society AIME, 1981, pp. 221-245.

33. Laser Surface Treatment of Metals, Draper, C., Mazzoldi, P., Martinus Nijhoff Publishers, Dordrechy, 1986, pp 297-308 and 369-388.

34. Cieslak, M., Headley, T., Frank, R., "The Welding Metallurgy of Custom Age 625 PLUS Alloy", Welding Research Supplement, Dec. 1989, pp 473-s-482-s.

35. Coutsouradis, D., Felix, P., Fischmeister, H., Habraken, L., Lindblom, Y., Speidel, M., "High Temperature Alloys for Gas Turbines", Applied Science Publishers LTD, London, 1978.

36. Thompson, R., "Microfissuring of Alloy 718 in the Weld Affected Zone", Journal of Metals, July 1988, pp 44-48.

37. Thompson, R., Mayo, D., Radhakrishnan, B., "The Relationship Between Carbon Content, Microstructure, and Intergranular Liquation Cracking in Cast Nickel Alloy 718", Metallurgical Transactions, Vol 22A, February 1991, pp 557-567.

38. Kelly, T., "Elemental Effects on Cast 718 Weldability", Welding Research Supplement, February 1989, pp 44-s - 51-s.

39. Kelly, T., Cremisio, W., Simon W., "An Evaluation of the Effects of Filler Metal Composition on Cast Alloy 718 Simulated Repair Welds", Welding Research Supplement, January 1989, pp 14-s - 18-s.

40. Busch, W., Kunze, H., "Microstructural Changes in the Heat Affected Zone of Precipitation Hardening Nickel-base Superalloys", Proceedings Material Development in Turbomachinery Design, Cambridge, UK, September 1988, pp 12-14.

41. Block-Bolten, A. and Eagar, T. "Metal Vaporization of Weld Pools", Metallurgical Transactions B, Vol 15B, September 1984, pp 461-469.

42. Khan, P. and Debroy, T., "Alloying Element Vaporization and Weld Pool Temperature During Laser Welding of AISI 202 Stainless Steel", Metallurgical Transactions B, Vol 15B, December 1984, pp 641-644.

43. David, S., Vitek, J., "Rapid Solidification Effects During Laser Welding", Proceedings ICALEO '91 Laser Material Processing, SPIE Vol 1722, pp 348-351.

44. Dey, G., Albert, S., Srivastava, D., Sundararaman, M., Mukhopadhyay, P., "Microstructural Studies on Rapidly Solidified Inconel 625", Materials Science Engineering, A119, 1989, pp 175-184.

45. Restall, J., Toulson, E., "Constitution and Microstructure of Certain Cast Nickel Superalloys", Metals and Materials, Vol 7, No. 3, March 1973, pp 134-139.

46. Hoffelner, W., Kny, E., Stickler, R., McCall, J., "Effects of Aging Treatments on the Microstructure of the Ni-Base Superalloy IN-738", Z. Werkstofftech, Vol 10, 1979, pp 84-92.

47. Wlodek, S., "SEM Metallography of Superalloys", Microstructural Science, Vol 18, pp 407-429.

48. Taha, M., Kurz, W., "About Microsegregation of Nickel Base Superalloys", Z. Metallkde, Vol 72, Aug. 1981, pp 546-549.

49. Quested, P., McLean, M., "Solidification Morphologies in Directionally Solidified Superalloys", Material Science Engineering, Vol 65, 1984, pp 171-180.

50. Ge, Y., Wang, J., "Transformation of MC Carbide in Cast Ni-Base Superalloys", Pract. Met., Vol 20, 1983, pp 554-561.

51. Koul, A., Gessinger, G., "On the Mechanism of Serrated Grain Boundary Formation in Ni-Based Superalloys", Acta Metall., Vol 31, No. 7, 1983, pp 1061-1069.

52. Piearcey, B., Kear, B., Smashey, R., "Correlation of Structure with Properties in a Directionally Solidified Nickel-Base Superalloy", Transactions of the ASM, Vol 60, 1967, pp 634-645.

53. Quested, P., McLean, M., Donner, A., Thyssen, G., Feingusswerk, B., "A Study of Directionally Solidified IN-738LC - Microstructure, Segregation and Mechanical Properties", Conference Proceedings, High Temperature Alloys for Gas Turbines and Other Applications, Oct. 1986, Liege, Belgium, pp 697-708.

54. David, S., Vitek, J., "Correlation Between Solidification Parameters and Weld Microstructures", International Materials Reviews, Vol 34, No. 5, 1989, pp 213-245.

55. Quantitative Microscopy, DeHoff, R., Rhines, F., McGraw-Hill Book Company, 1968.

56. Stevens, R., Flewitt, P., "Removal of Casting Porosity in Superalloy IN738 using Hidrostatic Pressure Sintering", Metal Science, March 1980, pp 81-88.

57. Stereological Methods, Vol 2, Weibel, E., Academic Press Inc. LTD, London, 1980.

58. Jahnke, B., "High-Temperature Electron Beam Welding of the Nickel-Base Superalloy IN-738 LC", Welding Journal, Nov. 1982, pp 343s-347s.

59. Van Drunen, G., Liburdi, J., Wallace, W., Terada, T. "Hot Isostatic Processing of IN-738 Turbine Blades", Agard Conference Proceedings No. 256, Advanced Fabrication Processes, Florence, Italy, 1978, pp 13-1 - 13-12.

60. Beddoes, J., Wallace, W., "Heat Treatment of Hot Isostatically Processed IN-738 Investment Castings", Metallography, Vol 13, 1980, pp 185-194.

61. Bacci, D., Tosto, S., "Surface Treatments by High Power Laser on Nickel Base Superalloys", Agard Conference Proceedings No. 256, Advanced Fabrication Processes, Florence, Italy, 1978, pp 9-1 - 9-10.

62. Haafkens, M., Matthey, J., "A New Approach to the Weldability of Nickelbase, As-cast and Powder Metallurgy Superalloys", (Agard) NATO Conference Proceedings, Jan. 1983, pp 14-1 - 14-13.